

Efficient calculation of carrier scattering rates from first principles

Alex M. Ganose,^{1,*} Junsoo Park,¹ Alireza Faghaninia,¹ Rachel Woods-Robinson,^{1,2} Kristin A. Persson,^{2,3} and Anubhav Jain^{1,†}

¹*Energy Technologies Area, Lawrence Berkeley National Laboratory, Berkeley, California 94720, USA*

²*Department of Materials Science and Engineering,*

University of California Berkeley, California 94720, United States

³*Molecular Foundry, Energy Sciences Area, Lawrence Berkeley National Laboratory, Berkeley, California 94720, USA*

(Dated: October 19, 2021)

The electronic transport behaviour of materials determines their suitability for technological applications. We develop a computationally efficient method for calculating carrier scattering rates of solid-state semiconductors and insulators from first principles inputs. The present method extends existing polar and non-polar electron-phonon coupling, ionized impurity, and piezoelectric scattering mechanisms formulated for isotropic band structures to support highly anisotropic materials. We test the formalism by calculating the electronic transport properties of 19 semiconductors, including the large 48 atom $\text{CH}_3\text{NH}_3\text{PbI}_3$ hybrid perovskite, and comparing the results against experimental measurements and more detailed scattering simulations. The Spearman rank coefficient of mobility against experiment ($r_s = 0.92$) improves significantly on results obtained using a constant relaxation time approximation ($r_s = 0.50$). We find our approach offers similar accuracy to state-of-the-art methods at approximately 1/500th the computational cost, thus enabling its use in high-throughput computational workflows for the accurate screening of carrier mobilities, lifetimes, and thermoelectric power.

Introduction

Solid-state materials exhibit a variety of electronic transport behaviors, enabling their deployment in a variety of technological applications, including light-emitting devices, photocatalysts, transparent conductors, solar cells, and thermoelectrics [1–6]. Recent years have seen an explosion of interest into the computational prediction of electronic transport properties, leading to a hierarchy of methods that can be broadly split into three categories. (i) Semi-empirical models for approximating electron lifetimes have been employed since the 1930s [7–12] but have seen a resurgence with the advent of large-scale materials science databases due to their computational efficiency [13–15]. These approaches have recently been extended to permit first-principles inputs [16–19] but the underlying assumption of single parabolic bands with no anisotropy limits their widespread application [20]. (ii) The second category eschews the calculation of electron lifetimes, instead employing a constant scattering rate for all electronic states. When combined with Fourier [21, 22] or Wannier [23] interpolation of *ab initio* electronic band structures this enables efficient calculation of transport properties in complex systems with multiple non-parabolic bands [24–26]. Recent work has applied this approach to compute the transport behaviour of large numbers of materials, including 48,000 semiconductors in the Materials Project database by Ricci *et al.* [27], 809 sulfides by Miyata *et al.* [28], and 75 potential thermoelectric candidates by Xing *et al.* [29]; however, the unphysical treatment of electron scattering and the reliance on an empirical tuning parameter often results in

significant errors. (iii) Finally, fully-first principles approaches to calculating the electron-phonon interaction based on density functional perturbation theory (DFPT) combined with Wannier interpolation can now yield highly accurate electron lifetimes and have demonstrated remarkable agreement to experimental measurements of electron mobility and conductivity [30–35]. The calculation of the scattering matrix elements needed to obtain electron lifetimes is extremely computationally demanding, even when approximations are made. With few exceptions [36–38], such approaches have been applied to highly symmetric systems with limited numbers of atoms. [39–44]. Although the computational cost of mobility calculations can be reduced through energy-averaging of the matrix elements [45], the initial DFPT calculation needed to obtain the matrix elements typically represents the majority of the computational expense. Despite the range of computational techniques available, no existing method can be applied to compute the transport properties of a broad array of complex materials both accurately and inexpensively [Fig. (2)]. This limitation is a primary obstacle in the application of high-throughput computations to the search for novel functional materials as well as applying this theory to larger and more complex materials.

In the present work, we develop an efficient formalism for calculating anisotropic transport properties of semiconductors that is accurate over a range of materials and amenable to use in high-throughput computational workflows. Our approach relies on inputs that can be obtained from low-cost *ab initio* methods and that are routinely available in computational materials science databases. Scattering rates are calculated using the momentum relaxation time approximation (MRTA) to the Boltzmann transport equation (BTE). The present method includes fully anisotropic acoustic deformation potential, piezo-

* aganose@lbl.gov

† ajain@lbl.gov

electric, ionized impurity, and polar electron-phonon scattering. As an initial test of the approach, we calculate the temperature-dependent electron mobility and Seebeck coefficient of 19 semiconductors including the large 48-atom $\text{CH}_3\text{NH}_3\text{PbI}_3$ hybrid perovskite. The Spearman rank coefficient of mobility against experiment ($r_s = 0.92$) improves significantly on results obtained using a constant relaxation time approximation ($r_s = 0.50$). Furthermore, we find our approach offers similar accuracy to state-of-the-art methods at 1/500th the computational cost. An open source software implementation of the method is made freely available.

Results

Computationally efficient matrix elements. In the Boltzmann transport equation, the scattering rate of an electron from an initial state $n\mathbf{k}$, where n is a band index and \mathbf{k} is a wave vector, to final state $m\mathbf{k} + \mathbf{q}$ is described by Fermi's golden rule as

$$\tau_{n\mathbf{k} \rightarrow m\mathbf{k} + \mathbf{q}}^{-1} = \frac{2\pi}{\hbar} |g_{nm}(\mathbf{k}, \mathbf{q})|^2 \delta(\varepsilon_{n\mathbf{k}} - \varepsilon_{m\mathbf{k} + \mathbf{q}}), \quad (1)$$

where \hbar is the reduced Planck constant, ε is the electron energy, δ is the Dirac delta function and g is the coupling matrix element. The above equation is given for the case of perfectly elastic scattering [46], in which no energy is gained or lost during the scattering process. A similar equation can be defined for inelastic processes (see Sec. I of the Supplemental Material), for instance to describe scattering that occurs via emission or absorption of a phonon. In the constant relaxation time approximation (CRTA), Eq. (1) is simplified to a single constant. In general, however, the impact of different scattering mechanisms is expressed via the coupling matrix element $g_{nm}(\mathbf{k}, \mathbf{q}) = \langle m\mathbf{k} + \mathbf{q} | \Delta_{\mathbf{q}} V | n\mathbf{k} \rangle$ where $\Delta_{\mathbf{q}} V$ is an electronic perturbation of some kind. The primary obstacle in obtaining accurate transport properties is evaluating $g_{nm}(\mathbf{k}, \mathbf{q})$ on extremely dense Brillouin zone grids, which has so far proven computationally prohibitive for all but the simplest systems [47, 48].

Historically, this challenge has been avoided by use of model matrix elements formulated for isotropic band structures using intrinsic materials parameters. For example, the treatment of deformation potential scattering due to long-wavelength acoustic phonons proposed by Bardeen and Shockley [8] depends only on an averaged elastic constant and band edge deformation potential;

it ignores perturbations from transverse phonon modes and anisotropy in the deformation response. This simple approach has been employed widely in computations of acoustic phonon scattering but is unreliable and does not generalise to complex systems or metals [49–51]. An alternative approach, developed by Khan and Allen [49], can reproduce the fully-first principles electron-phonon scattering rate if the strain tensor caused by the phonon and an additional velocity term are included. The resulting matrix element is given by

$$g_{nm}^{\text{KA}} = \langle m\mathbf{k} + \mathbf{q} | \mathbf{S}_{\mathbf{q}} : (\mathbf{D}_{n\mathbf{k}} + \mathbf{v}_{n\mathbf{k}} \otimes \mathbf{v}_{n\mathbf{k}}) | n\mathbf{k} \rangle, \quad (2)$$

where $:$ denotes the double dot product, $\mathbf{S}_{\mathbf{q}}$ is the strain associated with an acoustic phonon, $\mathbf{D}_{n\mathbf{k}}$ is the second rank deformation potential tensor and $\mathbf{v}_{n\mathbf{k}}$ is the group velocity. The velocity term is essential to correct the deformation potential in metals and at states away from the valence or conduction band edge in semiconductors. In practice, however, this equation is no longer simple to evaluate as it requires knowledge of the atomic displacements (the polarization direction) of the phonon mode in order to obtain the strain tensor.

In the present work, we combine the simplicity of the Bardeen and Shockley approach with the accuracy of the Khan and Allen matrix element by exploiting the acoustoelastic properties of materials. The dispersion relations for acoustic waves are contained in the Christoffel equation [52]

$$[\Gamma_{\hat{\mathbf{q}}} - \rho c^2 \mathbb{1}] \hat{\mathbf{u}} = 0, \quad (3)$$

where $\mathbb{1}$ is the identity matrix, $\hat{\mathbf{q}}$ and $\hat{\mathbf{u}}$ are unit vectors giving the direction of phonon propagation and polarization, respectively, ρ is the density, c is the wave velocity, and $\Gamma_{\hat{\mathbf{q}}} = \mathbf{C} \hat{\mathbf{q}} \cdot \hat{\mathbf{q}}$ is the Christoffel matrix where \mathbf{C} is the rank 4 elastic constant tensor. Solving the Christoffel equation for a phonon wave vector direction ($\hat{\mathbf{q}}$) results in three sets of eigenvalues (ρc^2) and eigenvectors ($\hat{\mathbf{u}}$), that correspond to the (quasi-)longitudinal and (quasi-)transverse normal modes of the material. The unit strain associated with each mode is given by $\hat{\mathbf{S}} = \hat{\mathbf{q}} \otimes \hat{\mathbf{u}}$ and the amplitude of the strain at any temperature T can be obtained from the potential energy of the acoustic phonon as $\sqrt{k_B T / \rho c^2}$, where k_B is the Boltzmann constant [53]. From this we arrive at an expression for acoustic deformation potential scattering (“ad”) that relies only on the deformation potentials and elastic constants and includes scattering from longitudinal and transverse modes in a single matrix element, given in the Born approximation [54] as

$$g_{nm}^{\text{ad}}(\mathbf{k}, \mathbf{q}) = \sqrt{k_B T} \sum_{\mathbf{G} \neq -\mathbf{q}} \left[\frac{\tilde{\mathbf{D}}_{n\mathbf{k}} : \hat{\mathbf{S}}_l}{c_l \sqrt{\rho}} + \frac{\tilde{\mathbf{D}}_{n\mathbf{k}} : \hat{\mathbf{S}}_{t_1}}{c_{t_1} \sqrt{\rho}} + \frac{\tilde{\mathbf{D}}_{n\mathbf{k}} : \hat{\mathbf{S}}_{t_2}}{c_{t_2} \sqrt{\rho}} \right] \langle m\mathbf{k} + \mathbf{q} | e^{i(\mathbf{q} + \mathbf{G}) \cdot \mathbf{r}} | n\mathbf{k} \rangle \quad (4)$$

where $\tilde{\mathbf{D}}_{n\mathbf{k}} = \mathbf{D}_{n\mathbf{k}} + \mathbf{v}_{n\mathbf{k}} \otimes \mathbf{v}_{n\mathbf{k}}$, and the subscripts l , t_1 ,

and t_2 indicate properties belonging to the longitudinal

and transverse modes.

Scattering by acoustic phonons through the piezoelectric interaction (“pi”) occurs in non-centrosymmetric systems and can dominate at low temperatures ($\lesssim 50$ K). We have applied a similar treatment to extend the isotropic

matrix element of Meijer and Polder [11], Harrison [55], and Zook [53], to include the full piezoelectric stress tensor \mathbf{h} and scattering from all three acoustic modes. The resulting matrix element is given by

$$g_{nm}^{\text{pi}}(\mathbf{k}, \mathbf{q}) = \sqrt{k_B T} \sum_{\mathbf{G} \neq -\mathbf{q}} \left[\frac{\hat{\mathbf{n}}\mathbf{h} : \hat{\mathbf{S}}_l}{c_l \sqrt{\rho}} + \frac{\hat{\mathbf{n}}\mathbf{h} : \hat{\mathbf{S}}_{t_1}}{c_{t_1} \sqrt{\rho}} + \frac{\hat{\mathbf{n}}\mathbf{h} : \hat{\mathbf{S}}_{t_2}}{c_{t_2} \sqrt{\rho}} \right] \frac{\langle m\mathbf{k} + \mathbf{q} | e^{i(\mathbf{q}+\mathbf{G}) \cdot \mathbf{r}} | n\mathbf{k} \rangle}{|\mathbf{q} + \mathbf{G}|}, \quad (5)$$

where $\hat{\mathbf{n}} = (\mathbf{q} + \mathbf{G})/|\mathbf{q} + \mathbf{G}|$ is a unit vector in the direction of scattering. Due to the small energies of long-wavelength acoustic phonons, both piezoelectric and acoustic deformation potential scattering describe a purely elastic process.

We treat polar optical phonon scattering (“po”) by extending the Frölich model [12] to include quantum mechanical wave function overlaps and anisotropic permittivity. Here, electrons in a dielectric medium are perturbed by a dispersionless longitudinal optical phonon mode with frequency ω_{po} . Our inelastic electron-phonon matrix element takes the form

$$g_{nm}^{\text{po}}(\mathbf{k}, \mathbf{q}) = \left[\frac{\hbar \omega_{\text{po}}}{2} \right]^{1/2} \sum_{\mathbf{G} \neq -\mathbf{q}} \left(\frac{1}{\hat{\mathbf{n}} \cdot \boldsymbol{\epsilon}_{\infty} \cdot \hat{\mathbf{n}}} - \frac{1}{\hat{\mathbf{n}} \cdot \boldsymbol{\epsilon}_s \cdot \hat{\mathbf{n}}} \right)^{\frac{1}{2}} \times \frac{\langle m\mathbf{k} + \mathbf{q} | e^{i(\mathbf{q}+\mathbf{G}) \cdot \mathbf{r}} | n\mathbf{k} \rangle}{|\mathbf{q} + \mathbf{G}|}, \quad (6)$$

where $\boldsymbol{\epsilon}_s$ and $\boldsymbol{\epsilon}_{\infty}$ are the static and high-frequency dielectric tensors. To capture scattering from the full phonon band structure in a single phonon frequency, each phonon mode is weighted by the dipole moment it produces (see Sec. III(A) of the Supplemental Material) in line with recent work that has rederived the Frölich model for systems with multiple phonon branches [56, 57]. Both our extension of the Frölich model and state-of-the-art first principles approaches produce similar matrix elements in the long-wavelength limit that dominates scattering (due to the polar singularity at $\mathbf{q} \rightarrow 0$ [56]).

Following the classic treatment of Brooks and Herring [9, 58] we consider the scattering from fully-ionized impurities (“ii”) modelled as screened Coulomb potentials, with the matrix element given by

$$g_{nm}^{\text{ii}}(\mathbf{k}, \mathbf{q}) = \sum_{\mathbf{G} \neq -\mathbf{q}} \frac{n_{\text{ii}}^{1/2} Z e}{\hat{\mathbf{n}} \cdot \boldsymbol{\epsilon}_s \cdot \hat{\mathbf{n}}} \frac{\langle m\mathbf{k} + \mathbf{q} | e^{i(\mathbf{q}+\mathbf{G}) \cdot \mathbf{r}} | n\mathbf{k} \rangle}{|\mathbf{q} + \mathbf{G}|^2 + \beta^2}, \quad (7)$$

where Z is the charge state of the impurity center, e is the electron charge, $n_{\text{ii}} = n_{\text{h}} + n_{\text{e}}$ is the concentration of ionized impurities, and β is the inverse screening length (defined in Sec. I(B) of the Supplemental Material). Unlike previous formulations, our matrix element accounts for anisotropy in the charge screening through use of the full dielectric tensor. Taken together, Eqs. (1) and (7) reveal

that the scattering almost diverges at long wavelengths ($\mathbf{q} \rightarrow 0$) due to a $1/|\mathbf{q}|^4$ dependence, and therefore requires very fine sampling to describe correctly. For this reason, even the most sophisticated methods for calculating electron scattering by ionized impurities employ the Brooks–Herring formula, in which Eq. (7) is analytically integrated for a single parabolic band [32, 59]. To overcome this limitation, we employ a modified linear-tetrahedron approach to integration, in which tetrahedron cross sections are numerically resampled with hundreds of extra points that exactly satisfy the delta term in Eq. (1). This allows for “effective” \mathbf{k} -point mesh densities that would be almost impossible to achieve with uniform \mathbf{k} -point sampling (the full methodology is provided in Sec. II(A) of the Supplemental Material). Our approach enables, for the first time, evaluation of Coulomb based impurity scattering in systems with multiple non-parabolic bands, which even more sophisticated approaches do not currently implement. In Sec. II(E) of the Supplemental Material, we demonstrate that our methodology reproduces the exact Brooks–Herring mobility for parabolic band structures and reveal the failure of the Brooks–Herring approach in the case of systems containing multiple anisotropic valleys.

The final \mathbf{k} -dependent scattering rates are obtained by integrating Eq. (1) over all phonon wave vectors (\mathbf{q}) in the first Brillouin zone. Elastic scattering processes are well described by the momentum relaxation time approximation (MRTA) to the BTE due to the requirement that $\tau_{n\mathbf{k} \rightarrow m\mathbf{k} + \mathbf{q}} = \tau_{m\mathbf{k} + \mathbf{q} \rightarrow n\mathbf{k}}$ [40]. As this condition does not hold for inelastic processes, we adopt the self-energy relaxation time approximation (SERTA) to obtain the final polar phonon coupling rates [32]. Further justification for this approach is detailed in Sec. I(A) of the Supplemental Material. Electronic eigenvalues and group velocities needed to calculate scattering and transport properties are Fourier interpolated onto dense Brillouin zone grids using the BOLTZTRAP2 software [22] (as detailed in Sec. II(A) of the Supplemental Material). Electron mobility and Seebeck coefficient are calculated using the linearized Boltzmann transport equation via the Onsager transport coefficients [22, 65] (see Sec. I(C) of the Supplemental Material). We also employ a custom procedure for selecting the most important \mathbf{k} -points at which to calculate scattering to further reduce the computational expense

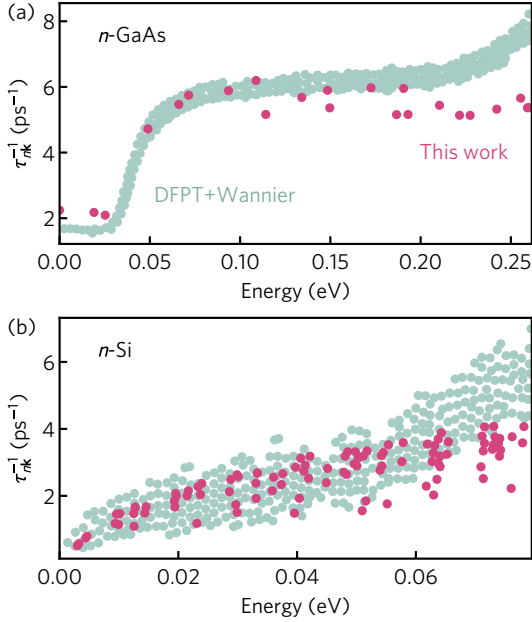


Fig. 1 — Comparison of the calculated scattering rates (pink) against those obtained using density functional perturbation theory combined with Wannier interpolation (light teal) for (a) n -GaAs [44] and (b) n -Si [32] at 300 K.

(detailed in Sec. II(B) of the Supplemental Material).

Unlike other state-of-the-art approaches in which a computationally expensive DFPT calculation is required to obtain $g(\mathbf{k}, \mathbf{q})$, in our method all matrix elements depend only on common materials parameters (ω_{po} , ϵ_s , ϵ_∞ , etc.) that can be calculated relatively inexpensively. Crucially, many of these properties are already tabulated in databases such as the Materials Project [66] or can be obtained through relatively cheap *ab initio* calculations. Furthermore, the matrix elements can be evaluated in a fixed time regardless of the number of atoms in the system, and multiple temperatures and carrier concentrations can be calculated simultaneously with only a modest increase in the computational time. Full timing information for the calculation of all first-principles inputs required to compute the transport properties of the materials discussed in this work and the scaling performance of each code routine is given in Sec. II(D) of the Supplemental Material.

Analysis of scattering rates and electron mobility. In Figure (1), we compare mode-dependent scattering rates for n -Si and n -GaAs calculated by our method against fully-first principles calculations (DFPT+Wannier) at 300 K obtained using the EPW and PERTURBO softwares [32, 35]. The scattering of electrons in Si is dominated by acoustic phonons whereas polar optical phonon scattering dominates in GaAs, as revealed by the mobility analysis in Sec. IV(B) in the Supplemental Material. Excellent agreement is seen for both systems, with the onset of polar optical emission scattering in GaAs well

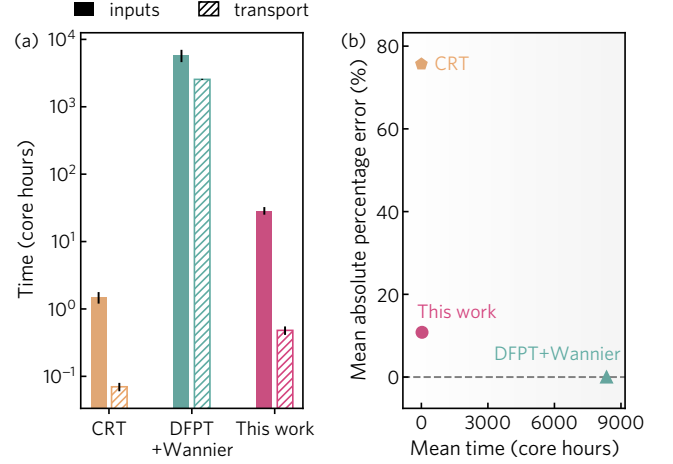


Fig. 2 — Existing methods for calculating electron transport properties are either computationally efficient but inaccurate (constant relaxation time, CRT) or accurate but highly computationally demanding (density functional perturbation theory combined with Wannier interpolation, DFPT+Wannier). The approach outlined in this work demonstrates accuracy comparable to state-of-the-art methods at approximately 1/500th the computational cost. (a) The time required to obtain electron mobility for each method is broken down by the time spent computing first-principles inputs and performing the scattering and transport calculations. (b) The mean absolute percentage error in the calculated mobility at 300 K is compared to the total computational time (including the time to obtain all first-principles inputs). Results are averaged for NbFeSb (p -type, $n = 2 \times 10^{20} \text{ cm}^{-3}$, DFPT+Wannier [39, 60]) and Ba_2BiAu (n -type, $n = 1 \times 10^{14} \text{ cm}^{-3}$, DFPT+Wannier [61]). In (b), the mobility error is referenced with respect to state-of-the-art DFPT+Wannier calculations as high-quality experimental data was not available. The full timing breakdown for each material is provided in Tables II and III in the Supplementary Material.

described by our calculations. Additional comparisons against DFPT+Wannier scattering rates for 3C-SiC and p -SnSe are provided in Fig. (S11) of the Supplemental Material. In both cases, the shape and magnitude of the scattering rates is well reproduced, particularly at low energies, despite the simpler approach that does not involve an expensive DFPT calculation to obtain the matrix elements.

In Fig. (2), we compare the time taken to compute the transport properties of NbFeSb and Ba_2BiAu (the full timing breakdown is tabulated in Tables II and III of the Supplemental Material). Taking into account the time required to compute all first-principles inputs and the electron mobility at a single temperature and carrier concentration, our method offers over a 2 order of magnitude speed up compared to DFPT+Wannier (an average of 29 core hours versus 8,350 core hours). Considering only the time needed to obtain the scattering rates and transport properties (i.e., presuming all inputs have already been tabulated), our approach offers a 4 order of magnitude speed up [Fig. (2a)]. This can be exploited when performing calculations at multiple temperatures and carrier concentrations. For example, calculating the mobility

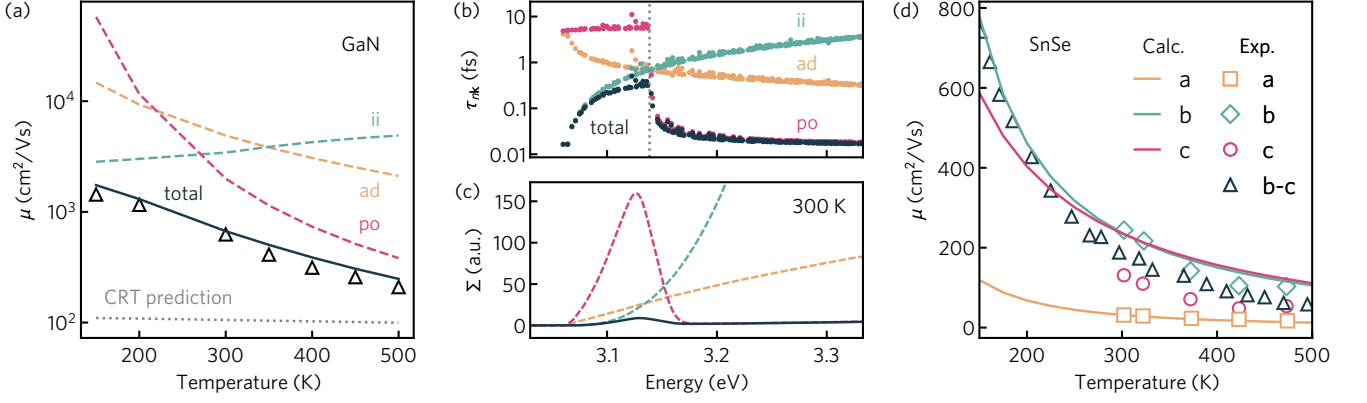


Fig. 3 | (a) Comparison of the electron mobility of GaN against experiment (black triangles, [62]). Mobility limited by ionized impurity (teal, “ii”), acoustic deformation potential (orange, “ad”), and polar optical phonon scattering (pink, “po”) is indicated in dashed lines. Total mobility taking into account all scattering mechanisms ($1/\tau_{nk}^{ii} + 1/\tau_{nk}^{ad} + 1/\tau_{nk}^{po}$) is given by the black solid line. Constant relaxation time (CRT) calculations with $\tau = 0.1$ fs is given by dotted gray line. (b) Electron lifetimes and (c) spectral conductivity arising from different scattering processes in GaN at 300 K. The valence band maximum is set to zero eV. In (b), the vertical dotted gray line indicates the energy of the effective polar phonon frequency, ω_{po} . (d) Comparison of the direction-dependent mobility of SnSe against experiments — a , b , c points from Ref. [63], b - c points from Ref. [64].

of Ba₂BiAu for 10 temperatures requires approximately 32,000 core hours using DFPT+Wannier compared to less than 35 core hours with our approach (95 % of which is required to calculate the first principles inputs). Furthermore, we expect the relative cost advantage of our method to increase with system size as unlike in DFPT+Wannier the computational expense of the matrix elements does not depend on the number of atoms. This reduction in computational time, combined with similar accuracy to DFPT+Wannier [within 10 %, see Fig. (2b)], makes our approach amenable to the large scale calculation of electronic transport properties.

Figure (3a) plots the calculated mobility of GaN against experimental measurements, indicating very close agreement from 150 K to 500 K. As each scattering mechanism is treated with a separate matrix element, this allows the impact of individual scattering processes to be assessed. At low temperatures, the mobility of GaN is limited by impurity scattering, with polar optical phonon scattering dominating above 300 K, as illustrated by the dashed lines in Fig. (3a). The total mobility taking into account all scattering mechanisms reproduces the experimental mobility with very high agreement. Further insight into the competing nature of the scattering mechanisms is provided by the energy dependence of the electron lifetimes and the resulting spectral conductivity, $\Sigma(\varepsilon) = v(\varepsilon)^2 \tau(\varepsilon) N(\varepsilon)$ where N is the density of states and v is the group velocity, computed at 300 K and an electron concentration of 5.5×10^{16} cm⁻³ [Figs. (3b) and (3c)]. Impurity scattering dominates at the conduction band edge but diminishes quickly as energy increases. At energies above ω_{po} of the band minimum (above the phonon emission threshold), polar-optical interactions are two orders of magnitude stronger than any other competing mechanism and act as the primary limiting factor for electron mobility, in agreement with the experimental findings of Ref. [67]

and DFPT+Wannier calculations [42]. In contrast, the mobility calculated using a constant relaxation time of $\tau = 0.1$ fs — a value on the higher end of that typically employed in screening studies [25, 26, 28] — underestimates the mobility by a factor of 2–10 depending on the temperature, as shown in Fig. (3a). More fundamentally, the CRTA does not reproduce the correct shape of temperature dependence as depicted in Fig. (3c). The ability of our method to reproduce the qualitative temperature dependence of transport properties, as well as make good approximations of quantitative behavior (often closely in-line with more detailed theoretical methods), thus represents a major advance for improving the accuracy of high-throughput methods.

A primary goal of the present approach is to extend well established scattering matrix elements that were formulated for isotropic materials properties to be compatible with highly anisotropic materials. To that end, we have calculated the direction-dependent hole mobilities of $Pnma$ structured SnSe at a carrier concentration of 3×10^{17} cm⁻³, with the results compared to Hall measurements in Fig. (3d). Single-crystal SnSe has recently attracted significant attention as a thermoelectric material. Due to its layered structure, SnSe exhibits anisotropic transport properties, with the highest thermoelectric performance observed along the b axis [63]. Our calculations reproduce the strong directional dependence in transport measurements, in which the mobility parallel to the layers (along b and c) is almost an order of magnitude larger than that perpendicular to the layers (along a). Our mobility results agree remarkably well with the considerably more computationally expensive electron-phonon calculations performed using DFPT+Wannier and $G0W0$ band structures [41] (see Fig. (S6) in the Supplemental Material). We note that additional anisotropy in the mobility between the b and c directions has been observed in high

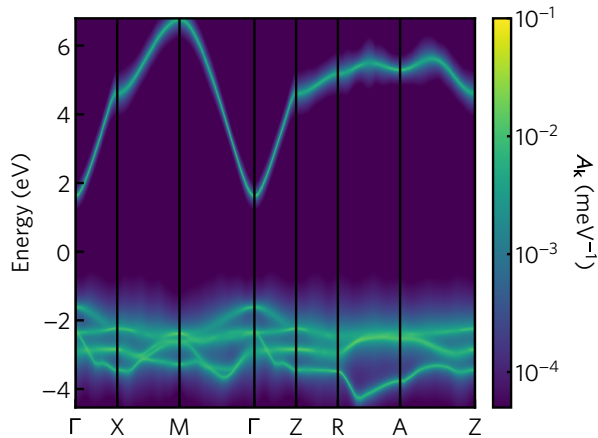


Fig. 4 — Spectral band structure of SnO_2 indicating band and \mathbf{k} -dependent electron linewidths calculated at 300 K.

temperature experimental measurements [63]. In both our calculations and DFPT+Wannier, however, the mobility along b and c are almost the same for temperatures above 300 K [41]. The discrepancy against experiment is thought to derive from the use of a Hall factor r_H of unity when extracting the carrier concentrations needed to compute mobility [41].

Access to band and \mathbf{k} -dependent lifetimes can further be used to calculate electron linewidths that are qualitatively comparable to those measured through techniques such as angle-resolved photoemission spectroscopy (ARPES) [68]. In Fig. (4) we plot the spectral band structure of SnO_2 along a high symmetry Brillouin zone path, where the spectral function $A_{\mathbf{k}}(\varepsilon) = \pi^{-1} \sum_n (\tau_{n\mathbf{k}}^{-1}/2) / [(\varepsilon - \varepsilon_{n\mathbf{k}}/\hbar)^2 + (\tau_{n\mathbf{k}}^{-1}/2)^2]$ was calculated at 300 K. The spectral function provides insight into the \mathbf{k} -dependence of the carrier lifetimes. States close to the conduction band edge at Γ exhibit long lifetimes (low energy broadening) due to the reduced phase space of available states for scattering. Between the Z and R high symmetry points, the lowest conduction band is relatively flat leading to large scattering rates and considerable broadening of the spectral function.

Electron mobility and Seebeck coefficient across many systems. To demonstrate the generality of our approach, we investigate the transport properties of 17 semiconductors ranging from 2 to 48 atoms in their primitive unit cells. To highlight the compatibility of the method with high-throughput computations, all inputs (eigenvalues, wave functions, materials parameters) are obtained from density functional theory (DFT) using low cost exchange–correlation functionals (see Methods section). All such materials parameters are listed in Table IV of in Supplemental Material. Results are compared to transport measurements on high purity single-crystalline samples to minimize the effects of grain boundaries and crystallographic defects. Further details on the calculation

methodology and selection of reference data are provided in Secs. II and III in the Supplemental Material. The materials span multiple chemistries, doping polarities, and band structure types including anisotropic and multiband systems, and comprise: (i) conventional semiconductors, Si, GaAs, GaN, GaP, InP, ZnS, ZnSe, CdS, CdSe, and SiC; (ii) the thermoelectric candidate SnSe; (iv) photovoltaic absorbers PbS and CdTe; and (iii) transparent conductors, SnO_2 , ZnO, and CuAlO_2 . Our dataset also includes the relatively complex $\text{CH}_3\text{NH}_3\text{PbI}_3$ hybrid perovskite containing 48-atoms. In Figure (5a) we compare calculated mobility against experimental measurements for all 17 materials in our dataset. Calculations were performed using the experimentally determined carrier concentrations at a temperature of 300 K. Results regarding the temperature and carrier concentration dependence of mobility for all materials (calculated, experimental, and comparison with CRTA) is provided in Figs. (S6) and (S7) of the Supplemental Material and include the breakdown of mobility by scattering type. These plots represent a comprehensive test of AMSET, across many materials, not only at the single condition plotted in Figure (5a) but when conditions are varied.

The calculated mobilities agree closely with experiment across all materials, covering several orders of magnitude from ZnO ($180 \text{ cm}^2/\text{Vs}$) to n -type GaAs ($\mu_{\text{exp}} = 2.1 \times 10^4 \text{ cm}^2/\text{Vs}$). Notably, the calculated mobility (Spearman rank coefficient against experiment $r_s = 0.92$) improves significantly on results obtained using a constant relaxation time approximation ($r_s = 0.50$). As we demonstrate in Fig. (S12) of the Supplemental Material, our method also improves the dependence of mobility on temperature, obtaining a mean squared error (MSE) of 0.21 consistent with DFPT+Wannier (MSE = 0.20) and dramatically more accurate than a constant relaxation time (MSE = 3.2). Greater deviation from experiment is observed for materials with smaller mobilities such as p - CuAlO_2 ($3 \text{ cm}^2/\text{Vs}$ in a - b plane), where a local hopping mechanism is proposed to compete with band transport [69], and p -CdTe in which spin–orbit coupling (SOC) is known to dramatically impact the scattering rates at the valence band edge [70] but was not included in our calculations. Additional deviation is observed for n -ZnS, where the calculated mobility is almost a factor of 4 larger than Hall measurements. We find this overestimation is largely due to the underestimation of the conduction band effective mass arising from use of the PBE exchange–correlation functional ($m_c^{*,\text{PBE}} = 0.16 m_e$) when compared to experiment ($m_c^{*,\text{exp}} = 0.22 m_e$) [71]. As we detail in Fig. (S8) of the Supplemental Material, calculations performed using the hybrid HSE06 functional result in a larger effective mass ($m_c^{*,\text{HSE}} = 0.20 m_e$) and improved agreement with the experimental mobility. Lastly, the deviation seen for $\text{CH}_3\text{NH}_3\text{PbI}_3$ is likely due to the use of polycrystalline thin films in experimental measurements. As highlighted by Fig. (S6) of the Supplemental Material, our temperature-dependent results are in excellent agreement (within 5% at all temperatures) against fully-first

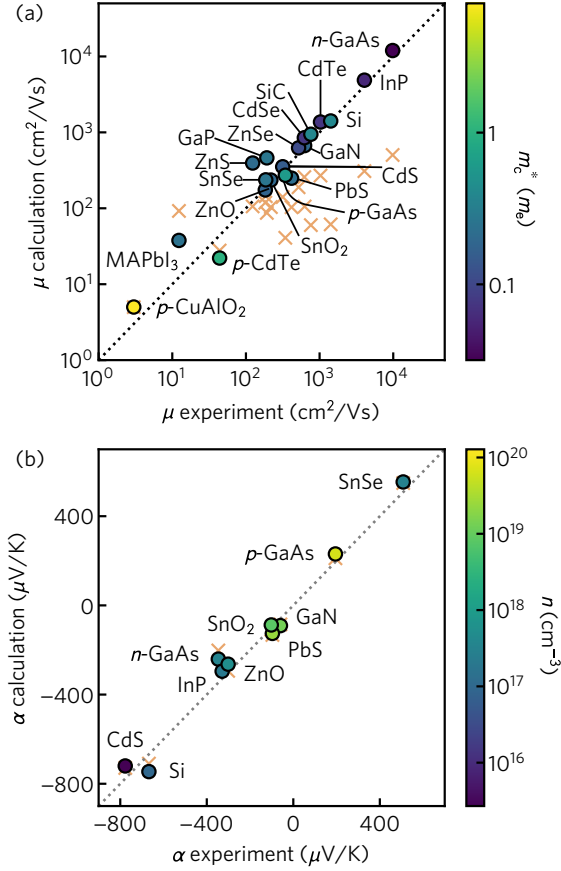


Fig. 5 — (a) Comparison of carrier mobilities at 300 K between calculations and experiments, with points colored by the conductivity effective mass m_c^* . (b) Comparison of Seebeck coefficients at 300 K between calculations and experiments, with points colored by the majority carrier concentration n . For Si and CdS we compare directly to the diffusive component of Seebeck coefficient only. $\text{CH}_3\text{NH}_3\text{PbI}_3$ has been abbreviated as MAPbI₃. In (a) and (b), orange crosses indicate results computed using a constant relaxation time of 0.1 fs. Detailed temperature and carrier concentration results for each material are provided in Sec. IV of the Supplemental Material.

principles calculations performed using EPW [37]. The ability of our approach to accurately describe the electron-phonon coupling of a highly complex structure with 144 phonon-modes while remaining computationally efficient highlights its potential in high-throughput screening of transport behaviour.

Accurate calculation of Seebeck coefficients is of primary interest in the prediction and analysis of thermoelectric materials. In Fig. (5b) we compare calculated Seebeck coefficients against those obtained experimentally at 300 K. A comparison of the temperature dependence of the Seebeck coefficient for all materials is provided in Fig. (S9) of the Supplemental Material. We see reasonable agreement against experiment across the full range of materials, for both p - and n -type samples, corresponding to positive and negative Seebeck coefficients, respectively. In the Fig. S10 of the Supplemental Material we demonstrate

that use of the HSE06 hybrid functional can further improve the agreement against experiment for n -type GaAs. We note that for Si and CdS we compare directly to the diffusive component of Seebeck coefficient only, ignoring the effects of phonon drag which contribute substantially even at room temperature [72–75]. The Seebeck coefficient displays a weaker dependence on electron lifetimes than mobility and conductivity and so is often treated within the CRTA (in which case the specific relaxation time cancels in the equations). [27]. Figure (5b) indicates that this approximation is often justified due to the relatively small disagreements between constant relaxation time and mode-dependent relaxation time results, in-line with previous comparisons of CRTA against experimental data [76].

Discussion

A key motivation in the development of the present approach is the opportunity to obtain accurate carrier lifetimes at minimal computational expense. Ideally, the method should be cheap enough to permit the calculation of transport properties for thousands of compounds in a high-throughput manner as well as large and complex materials. This would allow for reliable screening of materials for functional applications as well as enable investigations of systems with larger unit cells and more complex crystal structures. We stress that an expensive DFPT calculation is not required to obtain the matrix elements unlike methods such as EPW [30], PERTURBO [35], and EPIC STAR [45]. In our approach, the primary computational expense is the calculation of first-principles inputs, particularly the dielectric constant as detailed in Table II of the Supplemental Material. However, due to our use of the relatively low-cost PBE exchange–correlation functional all inputs (electronic structure, Γ -point phonon frequencies, elastic constants, dielectric constants and piezoelectric tensor) can be obtained with moderate computational requirements (generally less than 50 core hours to compute all properties, see Table II of the Supplemental Material). The calculation of transport properties takes even less time; the results for each material presented in this work — further timing analysis, indicating the breakdown for different routines in the code, is presented in Fig. (S4) of the Supplemental Material. In addition, many of the materials properties required to calculate the scattering matrix elements are already available in computational materials databases. For example, at the time of writing the Materials Project contains over 3,300 piezoelectric tensors, 7,100 dielectric constants and phonon frequencies, and over 13,000 elastic constants [66, 77, 78]. Accordingly, our approach is well suited for the large-scale analysis of transport properties. To that end, we have made available a Python implementation of the method called *Ab initio* Scattering and Transport (AMSET) at <https://github.com/hackingmaterials/amset>. Our goal is for this software to complement higher level methods, such as EPW [30] and PERTURBO [35], which are

state-of-the-art but considerably more computationally demanding. A schematic overview of the package, indicating the inputs, outputs and command-line tools is given in Fig. (S3) of the Supplemental Material.

We stress that all electronic dispersions and wave functions were computed using the PBE functional which tends to over-delocalise electronic states and underestimates effective masses. In most cases, the calculated mobility is overestimated compared to experiment, suggesting that use of higher level methods such as hybrid DFT or GW will be beneficial. In addition, there are several limitations of the current approach that may be addressed in a future release. In particular, optical deformation potential scattering is not treated, the symmetry of phonon modes is not used for filtering scattering events, and our matrix elements are not yet suitable for metals.

In conclusion, we introduced a method for calculating electron lifetimes and transport properties of semiconductors and insulators. Our method extends isotropic scattering matrix elements to support highly anisotropic materials and relies on a novel approach to Brillouin zone integration that overcomes the need for extremely dense \mathbf{k} -point sampling. The present approach offers similar accuracy to state-of-the-art methods at approximately 1/500th the computational cost and relies only on inputs that can be obtained from low-cost *ab initio* methods and that are routinely available in computational materials science databases. Furthermore, the agreement of mobility against experiment (Spearman rank coefficient $r_s = 0.92$) improves significantly on other low-cost methods such as a constant relaxation time approximation ($r_s = 0.50$) and temperature dependence is accurately captured. We expect that our method will enable accurate screening of transport properties in high-throughput computational workflows.

Methods

All DFT calculations were performed using the Perdew–Burke–Ernzerhof (PBE) exchange–correlation functional [79] as implemented in the Vienna *ab initio* Simulation Package (VASP) [80, 81]. Materials parameters, including elastic constants, dielectric tensors, deformation potentials, and phonon frequencies are listed in Table IV of in Supplemental Material. Calculations were performed in a plane-wave basis set with scalar relativistic pseudopotentials and with the interactions between core and valence electrons described using the projector augmented-wave method (PAW) [82, 83]. The set-up, submission, and management of first-principles calculations were handled using the ATOMATE workflow management software with the default parameters of version 0.8.3 [84, 85]. The plane-wave energy cutoff was set to 520 eV. Structure optimization was performed with a reciprocal \mathbf{k} -point density of 64 \mathbf{k} -points/Å³. The uniform non-self-consistent calculations used as input to the scattering calculations were run with a reciprocal \mathbf{k} -point density of 1000 \mathbf{k} -points/Å³. Band gaps are corrected using a scissor operation to

match those calculated by the Heyd–Scuseria–Ernzerhof (HSE06) hybrid functional [86, 87]. Piezoelectric constants, and static and high-frequency dielectric constants were computed using density functional perturbation theory (DFPT) based on the method developed and by Baroni and Resta [88] and adapted to the PAW formalism by Gajdoš *et al.* [89]. Elastic constants were obtained through the stress-strain approach detailed in Ref. [78]. Spin–orbit interactions were included for calculations on CH₃NH₃PbI₃ as they were necessary to obtain the correct band ordering at the conduction band minimum. A comparison of the experimental and HSE06 band gaps, along with initial and interpolated \mathbf{k} -point meshes are provided in Table V of the Supplemental Material. All timing information (first-principles inputs and transport properties) displayed in Fig. (2a) was obtained on an Intel Xeon Haswell processor E5-2698 v3 @ 2.3 GHz, except the EPW timing for NbFeSb. EPW timing information for NbFeSb was reported in Ref. [39] without specifying the processor type, so we have assumed a 1:1 correspondence in core performance.

Acknowledgments

This work was intellectually led and funded by the U.S. Department of Energy (DOE), Office of Basic Energy Sciences, Early Career Research Program. This research used resources of the National Energy Research Scientific Computing Center, which is supported by the Office of Science of the U.S. Department of Energy under Contract No. DEAC02-05CH11231. Lawrence Berkeley National Laboratory is funded by the DOE under award DE-AC02-05CH11231. We acknowledge fruitful discussions with K. Inzani and T. Karin.

References

- [1] S. Pimputkar, J. S. Speck, S. P. DenBaars, and S. Nakamura, Prospects for LED lighting, *Nat. Photonics* **3**, 180 (2009).
- [2] M. A. Green, A. Ho-Baillie, and H. J. Snaith, The emergence of perovskite solar cells, *Nat. Photonics* **8**, 506 (2014).
- [3] A. Fujishima and K. Honda, Electrochemical photolysis of water at a semiconductor electrode, *Nature* **238**, 37 (1972).
- [4] A. Jain, Y. Shin, and K. A. Persson, Computational predictions of energy materials using density functional theory, *Nat. Rev. Mater.* **1**, 1 (2016).
- [5] K. Ellmer, Past achievements and future challenges in the development of optically transparent electrodes, *Nat. Photonics* **6**, 809 (2012).
- [6] G. J. Snyder and E. S. Toberer, Complex thermoelectric materials, *Nat. Mater.* **7** (2008).
- [7] F. Bloch, Über die quantenmechanik der elektronen in kristallgittern, *Z. Phys.* **52**, 555 (1929).
- [8] J. Bardeen and W. Shockley, Deformation potentials and mobilities in non-polar crystals, *Phys. Rev.* **80**, 72 (1950).
- [9] C. Herring and E. Vogt, Transport and deformation-potential theory for many-valley semiconductors with anisotropic scattering, *Phys. Rev.* **101**, 944 (1956).

- [10] W. A. Harrison, Scattering of electrons by lattice vibrations in nonpolar crystals, *Phys. Rev.* **104**, 1281 (1956).
- [11] H. Meijer and D. Polder, Note on polar scattering of conduction electrons in regular crystals, *Physica* **19**, 255 (1953).
- [12] H. Fröhlich, Electrons in lattice fields, *Adv. Phys.* **3**, 325 (1954).
- [13] L. Xi, S. Pan, X. Li, Y. Xu, J. Ni, X. Sun, J. Yang, J. Luo, J. Xi, W. Zhu, *et al.*, Discovery of high-performance thermoelectric chalcogenides through reliable high-throughput material screening, *J. Amer. Chem. Soc.* **140**, 10785 (2018).
- [14] J. Yan, P. Gorai, B. Ortiz, S. Miller, S. A. Barnett, T. Mason, V. Stevanović, and E. S. Toberer, Material descriptors for predicting thermoelectric performance, *Energy Environ. Sci.* **8**, 983 (2015).
- [15] S. Wang, Z. Wang, W. Setyawan, N. Mingo, and S. Curtarolo, Assessing the Thermoelectric Properties of Sintered Compounds via High-Throughput *Ab-Initio* Calculations, *Phys. Rev. X* **1**, 021012 (2011).
- [16] A. Faghaninia, J. W. Ager III, and C. S. Lo, Ab initio electronic transport model with explicit solution to the linearized Boltzmann transport equation, *Phys. Rev. B* **91**, 235123 (2015).
- [17] A. K. Mandia, B. Muralidharan, J.-H. Choi, S.-C. Lee, and S. Bhattacharjee, AMMCR: Ab-initio model for mobility and conductivity calculation by using Rode Algorithm (2019), [arXiv:1907.08005 \[cond-mat.mtrl-sci\]](https://arxiv.org/abs/1907.08005).
- [18] A. S. Chaves, R. L. González-Romero, J. J. Meléndez, and A. Antonelli, Investigating charge carrier scattering processes in anisotropic semiconductors through first-principles calculations: The case of *p*-type SnSe (2020), [arXiv:2006.05506 \[cond-mat.mtrl-sci\]](https://arxiv.org/abs/2006.05506).
- [19] X. Li, Z. Zhang, J. Xi, D. J. Singh, Y. Sheng, J. Yang, and W. Zhang, TransOpt. A code to solve electrical transport properties of semiconductors in constant electron-phonon coupling approximation, *Computational Materials Science* **186**, 110074 (2021).
- [20] D. Long and J. Myers, Ionized-Impurity Scattering Mobility of Electrons in Silicon, *Phys. Rev.* **115**, 1107 (1959).
- [21] G. K. Madsen and D. J. Singh, BoltzTraP. a code for calculating band-structure dependent quantities, *Comput. Phys. Commun.* **175**, 67 (2006).
- [22] G. K. Madsen, J. Carrete, and M. J. Verstraete, BoltzTraP2, a program for interpolating band structures and calculating semi-classical transport coefficients, *Comput. Phys. Commun.* **231**, 140 (2018).
- [23] G. Pizzi, D. Volja, B. Kozinsky, M. Fornari, and N. Marzari, BoltzWann: A code for the evaluation of thermoelectric and electronic transport properties with a maximally-localized Wannier functions basis, *Comput. Phys. Commun.* **185**, 422 (2014).
- [24] E. B. Isaacs and C. Wolverton, Inverse Band Structure Design via Materials Database Screening: Application to Square Planar Thermoelectrics, *Chem. Mater.* **30**, 1540 (2018).
- [25] G. K. H. Madsen, Automated Search for New Thermoelectric Materials: The Case of LiZnSb, *J. Am. Chem. Soc.* **128**, 12140 (2006).
- [26] S. Bhattacharya and G. K. H. Madsen, A novel *p*-type half-Heusler from high-throughput transport and defect calculations, *J. Mater. Chem. C* **4**, 11261 (2016).
- [27] F. Ricci, W. Chen, U. Aydemir, G. J. Snyder, G.-M. Rignanese, A. Jain, and G. Hautier, An *ab initio* electronic transport database for inorganic materials, *Sci. Data* **4**, 170085 (2017).
- [28] M. Miyata, T. Ozaki, T. Takeuchi, S. Nishino, M. Inukai, and M. Koyano, High-Throughput Screening of Sulfide Thermoelectric Materials Using Electron Transport Calculations with OpenMX and BoltzTraP, *J. Electron. Mater.* **47**, 3254 (2018).
- [29] G. Xing, J. Sun, Y. Li, X. Fan, W. Zheng, and D. J. Singh, Electronic fitness function for screening semiconductors as thermoelectric materials, *Phys. Rev. Mater.* **1**, 065405 (2017).
- [30] S. Poncé, E. R. Margine, C. Verdi, and F. Giustino, EPW: Electron-phonon coupling, transport and superconducting properties using maximally localized Wannier functions, *Comput. Phys. Commun.* **209**, 116 (2016).
- [31] L. A. Agapito and M. Bernardi, Ab initio electron-phonon interactions using atomic orbital wave functions, *Phys. Rev. B* **97**, 235146 (2018).
- [32] S. Poncé, E. R. Margine, and F. Giustino, Towards predictive many-body calculations of phonon-limited carrier mobilities in semiconductors, *Phys. Rev. B* **97**, 121201 (2018).
- [33] X. Gonze, B. Amadon, G. Antonius, F. Arnardi, L. Baguet, J.-M. Beuken, J. Bieder, F. Bottin, J. Bouchet, E. Bousquet, *et al.*, The abinit project: Impact, environment and recent developments, *Comput. Phys. Commun.* **248**, 107042 (2020).
- [34] G. Brunin, H. P. C. Miranda, M. Giantomassi, M. Royo, M. Stengel, M. J. Verstraete, X. Gonze, G.-M. Rignanese, and G. Hautier, Phonon-limited electron mobility in Si, GaAs and GaP using plane waves and Bloch states (2020), [arXiv:2002.00630 \[cond-mat.mtrl-sci\]](https://arxiv.org/abs/2002.00630).
- [35] J.-J. Zhou, J. Park, I.-T. Lu, I. Maliyov, X. Tong, and M. Bernardi, Perturbo: a software package for ab initio electron-phonon interactions, charge transport and ultrafast dynamics (2020), [arXiv:2002.02045 \[cond-mat.mtrl-sci\]](https://arxiv.org/abs/2002.02045).
- [36] K. Ghosh and U. Singiseti, *Ab Initio* calculation of electron-phonon coupling in monoclinic β -Ga₂O₃ crystal, *Appl. Phys. Lett.* **109**, 072102 (2016).
- [37] S. Poncé, M. Schlipf, and F. Giustino, Origin of Low Carrier Mobilities in Halide Perovskites, *ACS Energy Lett.* **4**, 456 (2019).
- [38] W. Li, S. Poncé, and F. Giustino, Dimensional Crossover in the Carrier Mobility of Two-Dimensional Semiconductors: The Case of InSe, *Nano Lett.* **19**, 1774 (2019).
- [39] G. Samsonidze and B. Kozinsky, Accelerated screening of thermoelectric materials by first-principles computations of electron-phonon scattering, *Adv. Energy Mater.* **8**, 1800246 (2018).
- [40] S. Poncé, W. Li, S. Reichardt, and F. Giustino, First-principles calculations of charge carrier mobility and conductivity in bulk semiconductors and two-dimensional materials, *Rep. Prog. Phys.* **83**, 036501 (2020).
- [41] J. Ma, Y. Chen, and W. Li, Intrinsic phonon-limited charge carrier mobilities in thermoelectric SnSe, *Phys. Rev. B* **97**, 205207 (2018).
- [42] S. Poncé, D. Jena, and F. Giustino, Hole mobility of strained GaN from first principles, *Phys. Rev. B* **100**, 085204 (2019).

- [43] J. Cao, J. D. Querales-Flores, A. R. Murphy, S. Fahy, and I. Savić, Dominant electron-phonon scattering mechanisms in *n*-type PbTe from first principles, *Phys. Rev. B* **98**, 205202 (2018).
- [44] J.-J. Zhou and M. Bernardi, *Ab Initio* electron mobility and polar phonon scattering in GaAs, *Phys. Rev. B* **94**, 201201 (2016).
- [45] T. Deng, G. Wu, M. B. Sullivan, Z. M. Wong, K. Hippalgaonkar, J.-S. Wang, and S.-W. Yang, EPIC STAR: A reliable and efficient approach for phonon- and impurity-limited charge transport calculations, *npj Comput. Mater.* **6**, 46 (2020).
- [46] D. Rode, Low-field electron transport, in *Semiconductors and semimetals*, Vol. 10 (Elsevier, 1975) pp. 1–89.
- [47] F. Giustino, M. L. Cohen, and S. G. Louie, Electron-phonon interaction using Wannier functions, *Phys. Rev. B* **76**, 165108 (2007).
- [48] F. Giustino, Electron-phonon interactions from first principles, *Reviews of Modern Physics* **89**, 015003 (2017).
- [49] F. S. Khan and P. B. Allen, Deformation potentials and electron-phonon scattering: Two new theorems, *Phys. Rev. B* **29**, 3341 (1984).
- [50] E. Kartheuser and S. Rodriguez, Deformation potentials and the electron-phonon interaction in metals, *Phys. Rev. B* **33**, 772 (1986).
- [51] R. Resta, Deformation-potential theorem in metals and in dielectrics, *Phys. Rev. B* **44**, 11035 (1991).
- [52] B. Auld, Acoustic fields and waves in solids, Wiley Interscience Pub. , 278 (1973).
- [53] J. D. Zook, Piezoelectric Scattering in Semiconductors, *Phys. Rev.* **136**, A869 (1964).
- [54] M. Born, Quantenmechanik der stoßvorgänge, *Z. Phys.* **38**, 803 (1926).
- [55] W. A. Harrison, Mobility in zinc blende and indium antimonide, *Phys. Rev.* **101**, 903 (1956).
- [56] C. Verdi and F. Giustino, Fröhlich electron-phonon vertex from first principles, *Phys. Rev. Lett.* **115**, 176401 (2015).
- [57] J. Sjakste, N. Vast, M. Calandra, and F. Mauri, Wannier interpolation of the electron-phonon matrix elements in polar semiconductors: Polar-optical coupling in GaAs, *Phys. Rev. B* **92**, 054307 (2015).
- [58] H. Brooks, Scattering by ionized impurities in semiconductors, in *Phys. Rev.*, Vol. 83 (1951) pp. 879–879.
- [59] D. Chattopadhyay and H. Queisser, Electron scattering by ionized impurities in semiconductors, *Rev. Mod. Phys.* **53**, 745 (1981).
- [60] J. Zhou, H. Zhu, T.-H. Liu, Q. Song, R. He, J. Mao, Z. Liu, W. Ren, B. Liao, D. J. Singh, Z. Ren, and G. Chen, Large thermoelectric power factor from crystal symmetry-protected non-bonding orbital in half-Heuslers, *Nat. Commun.* **9**, 1721 (2018).
- [61] J. Park, Y. Xia, and V. Ozoliņš, High Thermoelectric Power Factor and Efficiency from a Highly Dispersive Band in Ba₂BiAu, *Phys. Rev. Applied* **11**, 014058 (2019).
- [62] C. Sułkowski, A. Chuchmała, A. J. Zaleski, M. Matusiak, J. Mucha, P. Głuchowski, and W. Stręk, Transport properties, specific heat and thermal conductivity of GaN nanocrystalline ceramic, *J. Solid State Chem.* **183**, 2501 (2010).
- [63] L.-D. Zhao, S.-H. Lo, Y. Zhang, H. Sun, G. Tan, C. Uher, C. Wolverton, V. P. Dravid, and M. G. Kanatzidis, Ultralow thermal conductivity and high thermoelectric figure of merit in SnSe crystals, *Nature* **508**, 373 (2014).
- [64] S. Asanabe, Electrical Properties of Stannous Selenide, *J. Phys. Soc. Jpn.* **14**, 281 (1959).
- [65] L. Onsager, Reciprocal relations in irreversible processes. I., *Phys. Rev.* **37**, 405 (1931).
- [66] A. Jain, S. P. Ong, G. Hautier, W. Chen, W. D. Richards, S. Dacek, S. Cholia, D. Gunter, D. Skinner, G. Ceder, *et al.*, Commentary: The Materials Project: A materials genome approach to accelerating materials innovation, *APL Mater.* **1**, 011002 (2013).
- [67] D. Steigerwald, S. Rudaz, H. Liu, R. S. Kern, W. Götz, and R. Fletcher, III–V nitride semiconductors for high-performance blue and green light-emitting devices, *Jom* **49**, 18 (1997).
- [68] C.-H. Park, F. Giustino, J. L. McChesney, A. Bostwick, T. Ohta, E. Rotenberg, M. L. Cohen, and S. G. Louie, Van Hove singularity and apparent anisotropy in the electron-phonon interaction in graphene, *Phys. Rev. B* **77**, 113410 (2008).
- [69] H. Kawazoe, M. Yasukawa, H. Hyodo, M. Kurita, H. Yanagi, and H. Hosono, P-type electrical conduction in transparent thin films of CuAlO₂, *Nature* **389**, 939 (1997).
- [70] D. Yadav, F. Pauly, and M. Trushin, Charge carrier thermalization in bulk and monolayer cdte: A first principles study (2019), [arXiv:1910.05216 \[cond-mat.mtrl-sci\]](https://arxiv.org/abs/1910.05216).
- [71] M. Nagano, H. Kanie, I. Yoshida, M. Sano, and M. Aoki, Photoluminescence in Sb-Doped ZnS, *Jpn. J. Appl. Phys.* **30**, 1915 (1991).
- [72] C. Herring, Theory of the thermoelectric power of semiconductors, *Phys. Rev.* **96**, 1163 (1954).
- [73] T. Geballe and G. Hull, Seebeck effect in silicon, *Phys. Rev.* **98**, 940 (1955).
- [74] M. Fiorentini and N. Bonini, Thermoelectric coefficients of *n*-doped silicon from first principles via the solution of the Boltzmann transport equation, *Phys. Rev. B* **94**, 085204 (2016).
- [75] K. Morikawa, Seebeck Effect in Cadmium Sulfide, *J. Phys. Soc. Jpn.* **20**, 786 (1965).
- [76] W. Chen, J.-H. Pöhls, G. Hautier, D. Broberg, S. Bajaj, U. Aydemir, Z. M. Gibbs, H. Zhu, M. Asta, G. J. Snyder, *et al.*, Understanding thermoelectric properties from high-throughput calculations: trends, insights, and comparisons with experiment, *J. Mater. Chem. C* **4**, 4414 (2016).
- [77] M. De Jong, W. Chen, H. Geerlings, M. Asta, and K. A. Persson, A database to enable discovery and design of piezoelectric materials, *Sci. Data* **2**, 1 (2015).
- [78] M. de Jong, W. Chen, T. Angsten, A. Jain, R. Notestine, A. Gamst, M. Sluiter, C. Krishna Ande, S. van der Zwaag, J. J. Plata, C. Toher, S. Curtarolo, G. Ceder, K. A. Persson, and M. Asta, Charting the complete elastic properties of inorganic crystalline compounds, *Sci. Data* **2**, 150009 (2015).
- [79] J. P. Perdew, K. Burke, and M. Ernzerhof, Generalized gradient approximation made simple, *Phys. Rev. Lett.* **77**, 3865 (1996).
- [80] G. Kresse and J. Furthmüller, Efficient iterative schemes for *ab initio* total-energy calculations using a plane-wave basis set, *Phys. Rev. B* **54**, 11169 (1996).

- [81] G. Kresse and J. Furthmüller, Efficiency of ab-initio total energy calculations for metals and semiconductors using a plane-wave basis set, *Comput. Mater. Sci.* **6**, 15 (1996).
- [82] P. E. Blöchl, Projector augmented-wave method, *Phys. Rev. B* **50**, 17953 (1994), [arXiv:1408.4701v2](#).
- [83] G. Kresse and D. Joubert, From ultrasoft pseudopotentials to the projector augmented-wave method, *Phys. Rev. B* **59**, 1758 (1999).
- [84] K. Mathew, J. H. Montoya, A. Faghaninia, S. Dwarakanath, M. Aykol, H. Tang, I. heng Chu, T. Smidt, B. Bocklund, M. Horton, J. Dagdelen, B. Wood, Z. K. Liu, J. Neaton, S. P. Ong, K. Persson, and A. Jain, Atomate: A high-level interface to generate, execute, and analyze computational materials science workflows, *Comput. Mater. Sci.* **139**, 140 (2017).
- [85] [Atomate v0.8.3](#) (2018).
- [86] J. Heyd, G. E. Scuseria, and M. Ernzerhof, Hybrid functionals based on a screened Coulomb potential, *J. Chem. Phys.* **118**, 8207 (2003).
- [87] J. Heyd, G. E. Scuseria, and M. Ernzerhof, Erratum:“Hybrid functionals based on a screened Coulomb potential”[*J. Chem. Phys.* 118, 8207 (2003)], *J. Chem. Phys.* **124**, 219906 (2006).
- [88] S. Baroni and R. Resta, *Ab Initio* calculation of the macroscopic dielectric constant in silicon, *Phys. Rev. B* **33**, 7017 (1986).
- [89] M. Gajdoš, K. Hummer, G. Kresse, J. Furthmüller, and F. Bechstedt, Linear optical properties in the projector-augmented wave methodology, *Phys. Rev. B* **73**, 045112 (2006), [arXiv:cond-mat/0510491](#)

Efficient calculation of electron scattering rates from first principles

Alex M. Ganose,¹ Junsoo Park,¹ Alireza Faghaninia,¹ Rachel Woods-Robinson,^{1,2} Kristin A. Persson,^{2,3} and Anubhav Jain¹

¹Energy Technologies Area, Lawrence Berkeley National Laboratory, Berkeley, California 94720, USA

²Department of Materials Science and Engineering,

University of California Berkeley, California 94720, United States

³Molecular Foundry, Energy Sciences Area, Lawrence Berkeley National Laboratory, Berkeley, California 94720, USA

(Dated: October 19, 2021)

I. THEORETICAL FRAMEWORK

A. Linearized Boltzmann transport equation

Electron mobility, μ_e , can be computed through the linearized Boltzmann transport equation (BTE) [1–4], given for electrons as

$$\mu_{e,\alpha\beta} = \frac{-1}{n_e\Omega} \sum_{n \in \text{cb}} \int \frac{d\mathbf{k}}{\Omega_{\text{BZ}}} v_{n\mathbf{k},\alpha} \partial_{E_\beta} f_{n\mathbf{k}}, \quad (\text{S1})$$

where α and β denote Cartesian coordinates, n_e is the electron concentration, Ω and Ω_{BZ} are the volumes of the unit cell and first Brillouin zone, respectively, $v_{n\mathbf{k},\alpha}$ is the group velocity of band index n and wave vector \mathbf{k} , “cb” stands for conduction bands, and $\partial_{E_\beta} f_{n\mathbf{k}}$ is the perturbation to the Fermi–Dirac distribution by an electric field \mathbf{E} . The Fermi–Dirac distribution is given by

$$f_{n\mathbf{k}}^0 = \frac{1}{\exp[(\varepsilon_{n\mathbf{k}} - \varepsilon_F)/k_B T] + 1}, \quad (\text{S2})$$

where $\varepsilon_{n\mathbf{k}}$ is the energy of state $n\mathbf{k}$, ε_F is the Fermi level, k_B is the Boltzmann constant, and T is temperature. The perturbation to the equilibrium Fermi–Dirac distribution is given by the self-consistent solution of

$$\begin{aligned} \partial_{E_\beta} f_{n\mathbf{k}} = & e \frac{\partial f_{n\mathbf{k}}^0}{\partial \varepsilon_{n\mathbf{k}}} v_{n\mathbf{k},\beta} \tau_{n\mathbf{k}} + \frac{2\pi\tau_{n\mathbf{k}}}{\hbar} \sum_m \int \frac{d\mathbf{q}}{\Omega_{\text{BZ}}} |g_{nm}(\mathbf{k}, \mathbf{q})|^2 \\ & \times [(n_{\mathbf{q}} + 1 - f_{n\mathbf{k}}^0) \delta(\Delta\varepsilon_{\mathbf{k},\mathbf{q}}^{nm} + \hbar\omega_{\mathbf{q}}) \\ & + (n_{\mathbf{q}} + f_{n\mathbf{k}}^0) \delta(\Delta\varepsilon_{\mathbf{k},\mathbf{q}}^{nm} - \hbar\omega_{\mathbf{q}})] \partial_{E_\beta} f_{m\mathbf{k}+\mathbf{q}}, \end{aligned} \quad (\text{S3})$$

where $\tau_{n\mathbf{k}}$ is the electron lifetime, δ is the Dirac delta function, $\Delta\varepsilon_{\mathbf{k},\mathbf{q}}^{nm} = \varepsilon_{n\mathbf{k}} - \varepsilon_{m\mathbf{k}+\mathbf{q}}$, \hbar is the reduced Planck constant, and $n_{\mathbf{q}}$ is the Bose–Einstein occupation. The matrix elements $g_{nm}(\mathbf{k}, \mathbf{q})$ give the probability of scattering from an initial state $n\mathbf{k}$ to final state $m\mathbf{k} + \mathbf{q}$ via a phonon with wave vector \mathbf{q} and frequency $\omega_{\mathbf{q}}$.

The primary complexity in the Boltzmann transport equation results from the dependence of the linear response coefficients $\partial_{E_\beta} f_{n\mathbf{k}}$ of state $n\mathbf{k}$ on all other states $m\mathbf{k} + \mathbf{q}$. Accordingly, there are several common approximations to the BTE that can significantly reduce the computational cost. The *momentum relaxation time approximation* (MRTA) makes two simplifications: (i) Firstly, the linear response coefficients are presumed to

only act in the direction of the band velocity, such that the electron lifetimes will be *scalar* quantities [2, 4]. (ii) Secondly, the probability of scattering from state $n\mathbf{k}$ to $m\mathbf{k} + \mathbf{q}$ is assumed to be the same as scattering from state $m\mathbf{k} + \mathbf{q}$ to $n\mathbf{k}$. The result is that the effects of back scattering are accounted for by a geometrical factor resulting from the electronic group velocities. The resulting expression for $\tau_{n\mathbf{k}}^{-1}$ can be written

$$\tau_{n\mathbf{k}}^{-1} = \sum_m \int \frac{d\mathbf{q}}{\Omega_{\text{BZ}}} \left[1 - \frac{\mathbf{v}_{n\mathbf{k}} \cdot \mathbf{v}_{m\mathbf{k}+\mathbf{q}}}{|\mathbf{v}_{n\mathbf{k}}|^2} \right] \tau_{n\mathbf{k} \rightarrow m\mathbf{k}+\mathbf{q}}^{-1}, \quad (\text{S4})$$

where $\tau_{n\mathbf{k} \rightarrow m\mathbf{k}+\mathbf{q}}^{-1}$ is the partial decay rate for scattering from initial state $n\mathbf{k}$ to final state $m\mathbf{k} + \mathbf{q}$. In this approximation, Eq. (S1) can be rewritten

$$\mu_{e,\alpha\beta}^{\text{MRTA}} = \frac{e}{n_e\Omega} \sum_{n \in \text{cb}} \int \frac{d\mathbf{k}}{\Omega_{\text{BZ}}} \frac{\partial f_{n\mathbf{k}}^0}{\partial \varepsilon_{n\mathbf{k}}} v_{n\mathbf{k},\alpha} v_{n\mathbf{k},\beta} \tau_{n\mathbf{k}}. \quad (\text{S5})$$

A further simplification can be made by ignoring the effects of scattering back into the state $n\mathbf{k}$ entirely. This corresponds to neglecting the second term on the right-hand side of Eq. (S3) or setting the geometric factor in the square bracket of Eq. (S4) to 1. In this approach, termed the *self-energy relaxation time approximation* (SERTA) [3], the electron lifetimes can be obtained according to

$$\tau_{n\mathbf{k}}^{-1} = \sum_m \int \frac{d\mathbf{q}}{\Omega_{\text{BZ}}} \tau_{n\mathbf{k} \rightarrow m\mathbf{k}+\mathbf{q}}^{-1}, \quad (\text{S6})$$

and the mobility calculated in the same manner as Eq. (S5).

The partial decay rates of Eqs. (S4) and (S6) can be obtained through Fermi’s golden rule. In the present work, we implement two classes of scattering: (i) inelastic scattering which occurs via emission or absorption of a phonon and (ii) perfectly elastic scattering in which no energy is gained or lost. In the case of inelastic scattering, the partial decay rate can be written [5, 6]

$$\begin{aligned} \tau_{n\mathbf{k} \rightarrow m\mathbf{k}+\mathbf{q}}^{-1} = & \frac{2\pi}{\hbar} |g_{nm}(\mathbf{k}, \mathbf{q})|^2 \\ & \times [(n_{\mathbf{q}} + 1 - f_{m\mathbf{k}+\mathbf{q}}^0) \delta(\Delta\varepsilon_{\mathbf{k},\mathbf{q}}^{nm} - \hbar\omega_{\mathbf{q}}) \\ & + (n_{\mathbf{q}} + f_{m\mathbf{k}+\mathbf{q}}^0) \delta(\Delta\varepsilon_{\mathbf{k},\mathbf{q}}^{nm} + \hbar\omega_{\mathbf{q}})], \end{aligned} \quad (\text{S7})$$

where the $-\hbar\omega_{\mathbf{q}}$ and $+\hbar\omega_{\mathbf{q}}$ terms correspond to scattering by emission and absorption of a phonon, respectively. The dependence of $\tau_{n\mathbf{k} \rightarrow m\mathbf{k}+\mathbf{q}}^{-1}$ on the occupation

TABLE I. Summary of scattering mechanisms

Name	Required properties	Type	Refs.
Ionized impurity	Static dielectric	Elastic	[7, 8]
Acoustic deformation potential	Deformation potential, elastic constant	Elastic	[9–12]
Piezoelectric acoustic	Piezoelectric constant	Elastic	[13–15]
Polar optical phonon	Static and high-frequency dielectric, phonon frequency	Inelastic	[16]

of state $m\mathbf{k} + \mathbf{q}$ and the observation that $f_{m\mathbf{k}+\mathbf{q}} \neq f_{n\mathbf{k}}$ reveals that inelastic scattering is not commutative — i.e., $\tau_{n\mathbf{k} \rightarrow m\mathbf{k}+\mathbf{q}}^{-1} \neq \tau_{m\mathbf{k}+\mathbf{q} \rightarrow n\mathbf{k}}^{-1}$. We note that for spin polarized materials, scattering only occurs between states in the same spin channel — i.e., there are no interactions between spin-up and spin-down electrons.

For elastic scattering, Eq. (S7) reduces to

$$\tau_{n\mathbf{k} \rightarrow m\mathbf{k}+\mathbf{q}}^{-1} = \frac{2\pi}{\hbar} |g_{nm}(\mathbf{k}, \mathbf{q})|^2 \delta(\Delta\varepsilon_{\mathbf{k},\mathbf{q}}^m). \quad (\text{S8})$$

In contrast to inelastic scattering, elastic processes do not depend on the occupation of state $m\mathbf{k} + \mathbf{q}$. Accordingly, $\tau_{n\mathbf{k} \rightarrow m\mathbf{k}+\mathbf{q}}^{-1} = \tau_{m\mathbf{k}+\mathbf{q} \rightarrow n\mathbf{k}}^{-1}$ and a primary assumption of the MRTA is satisfied. For this reason, we treat elastic scattering processes under the MRTA, whereas inelastic scattering processes are treated in the SERTA.

B. Scattering matrix elements

The general form of the quantum mechanical scattering matrix elements in Eqs. (S3), (S4), and (S6) is

$$g_{nm}(\mathbf{k}, \mathbf{q}) = \langle m\mathbf{k} + \mathbf{q} | \Delta_{\mathbf{q}} V | n\mathbf{k} \rangle \quad (\text{S9})$$

where $\Delta_{\mathbf{q}} V$ is an electronic perturbation associated with a scattering process [6]. In the present work we calculate matrix elements within the Born approximation [17]; namely, the electronic perturbation is assumed to only weakly impact the wave function of the final state $m\mathbf{k} + \mathbf{q}$. The scattering matrix elements considered in this work and the materials parameters needed to calculate them are summarized in Table I.

1. *G*-vector summation

The matrix elements include a sum over reciprocal lattice vectors \mathbf{G} . In this work, we restrict the summation to only include a single reciprocal lattice vector, $\mathbf{G}_{\mathbf{q}}$, such

that $|\mathbf{q} + \mathbf{G}_{\mathbf{q}}| = \min_{\mathbf{G}} |\mathbf{q} + \mathbf{G}_{\mathbf{q}}|$. This corresponds to retaining only the handful of $\mathbf{G} + \mathbf{q}$ vectors that define the first Brillouin zone.

2. Impurity scattering

The inverse screening length β , required in the calculation of the ionized impurity matrix element, is given by

$$\beta^2 = \frac{e^2}{\epsilon_s k_B T \Omega} \sum_n \int f_{n\mathbf{k}}^0 (1 - f_{n\mathbf{k}}^0) d\mathbf{k}, \quad (\text{S10})$$

where $1/\beta$ corresponds to the Debye length and Thomas–Fermi screening length for non-degenerate and degenerate doping regimes, respectively [18].

C. Transport properties

Electronic transport properties — namely, conductivity, Seebeck coefficient, and electronic component of thermal conductivity — are calculated through the Onsager coefficients [19, 20]. The spectral conductivity, defined as

$$\Sigma_{\alpha\beta}(\varepsilon) = \sum_n \int \frac{d\mathbf{k}}{8\pi^3} v_{n\mathbf{k},\alpha} v_{n\mathbf{k},\beta} \tau_{n\mathbf{k}} \delta(\varepsilon - \varepsilon_{n\mathbf{k}}), \quad (\text{S11})$$

is used to compute the moments of the generalized transport coefficients

$$\mathcal{L}_{\alpha\beta}^n = e^2 \int \Sigma_{\alpha\beta}(\varepsilon) (\varepsilon_F - \varepsilon)^n \left[-\frac{\partial f^0}{\partial \varepsilon} \right] d\varepsilon, \quad (\text{S12})$$

where ε_F is the Fermi level at a certain doping concentration and temperature T . Electrical conductivity (σ), Seebeck coefficient (S), and the charge carrier contribution to thermal conductivity (κ) are obtained as

$$\sigma_{\alpha\beta} = \mathcal{L}_{\alpha\beta}^0, \quad (\text{S13})$$

$$S_{\alpha\beta} = \frac{1}{eT} \frac{\mathcal{L}_{\alpha\beta}^1}{\mathcal{L}_{\alpha\beta}^0}, \quad (\text{S14})$$

$$\kappa_{\alpha\beta} = \frac{1}{e^2 T} \left[\frac{(\mathcal{L}_{\alpha\beta}^1)^2}{\mathcal{L}_{\alpha\beta}^0} - \mathcal{L}_{\alpha\beta}^2 \right]. \quad (\text{S15})$$

II. COMPUTATIONAL FRAMEWORK

A. Brillouin-zone interpolation and integration

As described in the main text, we employ a combined Fourier-linear interpolation scheme when calculating scattering and transport properties. Electronic eigenvalues — calculated using density functional theory (DFT) on a coarse \mathbf{k} -point mesh — are Fourier interpolated onto a denser mesh. Fourier interpolation is

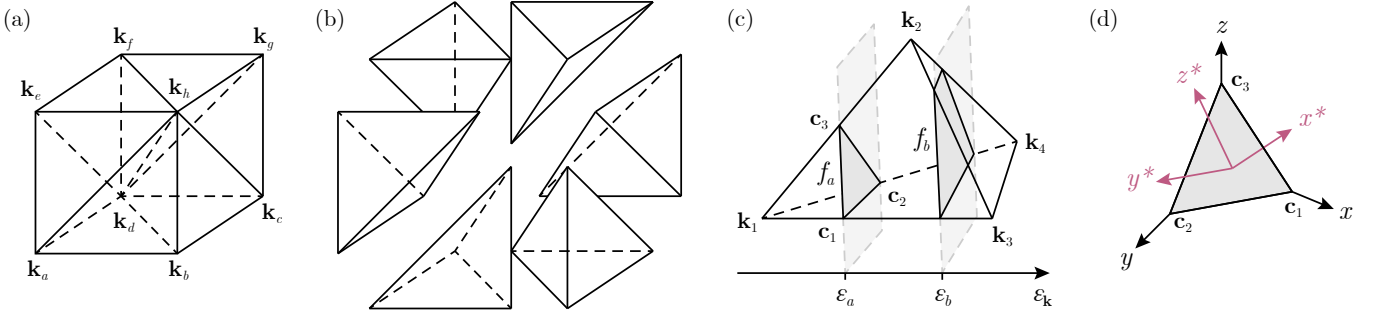


FIG. S1. Schematic of the linear-tetrahedron method. (a) A $2 \times 2 \times 2$ \mathbf{k} -point submesh can be broken up into (b) six tetrahedra. Adapted from Ref. [21]. (c) The constant energy surfaces (light gray planes) defined by ε_a and ε_b intersect the tetrahedron to produce the cross sections f_a (dark gray triangle) and f_b (dark gray quadrangle). The triangular cross section f_a is defined by the points \mathbf{c}_1 , \mathbf{c}_2 , and \mathbf{c}_3 . The \mathbf{k} -points at the tetrahedron vertices have been numbered according to increasing energy, i.e., $\varepsilon_{\mathbf{k}_1} < \varepsilon_{\mathbf{k}_2} < \varepsilon_{\mathbf{k}_3} < \varepsilon_{\mathbf{k}_4}$. (d) Coordinate transformation from initial basis (black arrows) to transformed basis (pink arrows) that maps the cross section onto a 2D plane. The x^* coordinates of all points on the cross section are zero.

performed using the BOLTZTRAP2 software [22, 23] which enforces symmetry using star functions and employs the Shankland algorithm to ensure that both quasi-particle energies and their derivatives (group velocities) are exactly reproduced [24–26]. This approach aims to minimise the roughness function proposed in Ref. [27].

Scattering rates are calculated on the Fourier interpolated \mathbf{k} -point mesh. When calculating the partial decay rate, scattering is limited to the constant energy surface defined by $\varepsilon = \varepsilon_{n\mathbf{k}}$ in the case of elastic processes [Eq. (S8)] and $\varepsilon = \varepsilon_{n\mathbf{k}} \pm \hbar\omega_{\mathbf{q}}$ for inelastic processes [Eq. (S7)]. Note that, in our implementation of polar optical phonon scattering we rely on a single dispersionless phonon mode, whose energy $\hbar\omega_{\text{po}}$ is independent of \mathbf{q} . Due to finite \mathbf{k} -point sampling, it is common to replace the delta function in Eqs. (S7) and (S8) by Gaussian or Lorentzian functions with finite broadening. This procedure has the effect that the calculated lifetimes will depend on the chosen broadening parameter.

An alternative approach is to employ the linear tetrahedron method to analytically integrate the scattering rates across the constant energy surface [21, 28]. In this method, the Brillouin zone is divided into tetrahedra [Figs. S1(a) and S1(b)]. For each electronic band, the eigenvalues are obtained for the \mathbf{k} -points at the corners of the tetrahedra. The constant energy surface defined by $\varepsilon_{n\mathbf{k}}$ intersects a tetrahedron if $\varepsilon_{\text{tetra}}^{\min} < \varepsilon_{n\mathbf{k}} < \varepsilon_{\text{tetra}}^{\max}$, where $\varepsilon_{\text{tetra}}^{\min}$ and $\varepsilon_{\text{tetra}}^{\max}$ are the minimum and maximum energies of the tetrahedron’s vertices [Fig. S1(c)]. Computing the intersections of $\varepsilon_{n\mathbf{k}}$ with all tetrahedra gives rise to a set of tetrahedron cross-sections that define the constant energy surface. In the traditional implementation of the tetrahedron method, the integration for each tetrahedron is performed analytically after linearly interpolating the eigenvalues and matrix elements inside the tetrahedron. As we note in the main text, this approach is only valid for matrix elements that show a linear dependence on \mathbf{q} . For ionized impurity scattering, where the matrix element has a $1/|\mathbf{q}|^2$ dependence, this assumption

does not hold and results in severe overestimation of the scattering rate.

To overcome this limitation, we employ a modified linear-tetrahedron approach. The constant energy surface is determined in the same manner as the tetrahedron method. However, instead of analytically integrating within each tetrahedra, the tetrahedron cross sections (comprising the constant energy surface) are numerically resampled with hundreds of extra points. By only computing additional \mathbf{k} -points that exactly satisfy the delta term in Eqs. (S7) and (S8), this allows for “effective” \mathbf{k} -point mesh densities that would be almost impossible to achieve with uniform \mathbf{k} -point sampling. The scattering matrix elements are computed on the denser submesh by linear interpolation of the electronic wave functions $\psi_{n\mathbf{k}}$ and group velocities $\mathbf{v}_{n\mathbf{k}}$. We note that the scattering wave vector \mathbf{q} is a geometric term that is known exactly for all points on the submesh. A primary advantage of this approach is that while the matrix elements cannot be linearly interpolated with \mathbf{q} , the constituent parameters (electronic wave functions and group velocities) are linearly interpolatable.

In order to resample the constant energy surface, the tetrahedron cross sections are projected onto a two-dimensional plane. First, the \mathbf{k} -points that define the tetrahedron cross sections are identified. These are the points at the intersection of the constant energy surface and tetrahedron boundary under the assumption that the band energies vary linearly between adjacent vertices in the tetrahedron [points labelled \mathbf{c} in Fig. S1(c)]. This results in three and four sets of \mathbf{k} -points for triangular and quadrilateral cross sections, respectively, termed \mathbf{C} . The first basis vector for the new coordinate system, \mathbf{B} , is the vector normal to the plane of the cross section, namely

$$\mathbf{b}_1 = \frac{\mathbf{c}_2 - \mathbf{c}_1}{|\mathbf{c}_2 - \mathbf{c}_1|} \times \frac{\mathbf{c}_3 - \mathbf{c}_1}{|\mathbf{c}_3 - \mathbf{c}_1|},$$

where \mathbf{c}_1 and \mathbf{c}_2 are the coordinates of the first and second vertices defining the cross section. The second and

third basis vectors are defined as

$$\mathbf{b}_2 = \frac{\mathbf{c}_2 - \mathbf{c}_1}{|\mathbf{c}_2 - \mathbf{c}_1|},$$

$$\mathbf{b}_3 = \mathbf{b}_2 \times \mathbf{b}_1,$$

The reciprocal space coordinates defining the cross section are transformed onto the new basis through

$$\mathbf{c}_i^{\text{proj}} = \mathbf{B}^{-1} \cdot \mathbf{c}_i.$$

In the new coordinate system, the first component of all coordinates will be the same, as all vertices lie on a plane. The last two components of the coordinates define a two-dimensional (2D) projection of the cross section which can be resampled through numerical quadrature schemes [Fig. S1(d)]. In the present work, we employ degree 50 Xiao–Gimbutas (containing 453 sample points, [29]) or Festa–Sommariva quadratures (454 points, [30]) for resampling triangular and quadrilateral tetrahedron cross-sections, respectively. Resampling, including generating sample points and integration weights w_i^{res} , is performed using the QUADPY software [31]. The set of sample points are transformed back into the original coordinate system through

$$\mathbf{c}_i = \mathbf{B} \cdot \mathbf{c}_i^{\text{proj}}.$$

The contribution of each tetrahedron to the constant energy surface is weighted by a geometric factor that accounts for the tetrahedron’s shape in four dimensional space (reciprocal coordinates and energy space) [28]. Using the triple \mathbf{r}_i contragradient to vertices of the tetrahedron \mathbf{k}_i

$$\mathbf{r}_i \mathbf{k}_i = \delta_{ij},$$

$$\mathbf{r}_1 = \frac{\mathbf{k}_3 \times \mathbf{k}_4}{\Omega},$$

$$\mathbf{r}_2 = \frac{\mathbf{k}_4 \times \mathbf{k}_2}{\Omega},$$

$$\mathbf{r}_3 = \frac{\mathbf{k}_2 \times \mathbf{k}_3}{\Omega},$$

where the \mathbf{k} -points have been numbered according to increasing energy, i.e., $\varepsilon_{\mathbf{k}_1} < \varepsilon_{\mathbf{k}_2} < \varepsilon_{\mathbf{k}_3} < \varepsilon_{\mathbf{k}_4}$, the tetrahedron weight is given by [28]

$$w^{\text{tet}} = \left| \sum_{i=2}^4 (\varepsilon_{\mathbf{k}_i} - \varepsilon_{\mathbf{k}_1}) \mathbf{r}_{i-1} \right|^{-1}.$$

We stress that this weight is distinct from the integration weights defined by Blöchl *et al.* [21] in which the contragradient cancels when averaging over all adjacent tetrahedra. The final integration weights w_i for the sample \mathbf{k} -point coordinates of each cross section are scaled by the tetrahedron weight to give $w_i = w_i^{\text{res}} \cdot w^{\text{tet}}$.

When evaluating the density of states

$$N(\varepsilon) = \sum_n \int \frac{d\mathbf{k}}{8\pi^3} \delta(\varepsilon - \varepsilon_{n\mathbf{k}}), \quad (\text{S16})$$

and the spectral conductivity in Eq. (S11), we employ the traditional approach to the linear-tetrahedron method described by Blöchl *et al.* [21]. Specifically, we use the energy-dependent integration weights as described in Ref. [32] and elsewhere. Unlike the partial decay rates $\tau_{n\mathbf{k} \rightarrow m\mathbf{k} + \mathbf{q}^{-1}}$, the final lifetimes $\tau_{n\mathbf{k}}$ vary smoothly across the Brillouin zone. Accordingly, use of the linear-tetrahedron method can significantly improve the convergence of transport properties without issue.

B. Optimization of scattering calculations

Under typically achievable carrier concentrations (10^{16} to 10^{21} cm^{-3} /Vs) the Fermi level will sit close to either the conduction or valence band edge. Accordingly, only \mathbf{k} -points that lie within a few hundred meV of the band edge will contribute to electronic transport. It is therefore unnecessary to compute the electron lifetimes for all \mathbf{k} -points in the band structure, as most will have no impact on transport properties. From the generalized transport coefficients \mathcal{L} in Eq. (S12), it can be seen that each \mathbf{k} -point’s contribution to the transport properties is scaled by a factor $(\varepsilon_{n\mathbf{k}} - \varepsilon_F)^n [-\partial f_{n\mathbf{k}}^0 / \partial \varepsilon_{n\mathbf{k}}]$, which depends entirely on the energy of the state. Accordingly, we have designed a procedure to assess which energy range is important for transport, illustrated in Fig. S2(a). We begin by denoting the “moment-coefficient weight” as

$$w_n(\varepsilon) = (\varepsilon_F - \varepsilon)^n \left[-\frac{\partial f^0}{\partial \varepsilon} \right], \quad (\text{S17})$$

where the indices $n = 0, 1, 2$, correspond to the moments of \mathcal{L}^n required to compute conductivity, Seebeck coefficient, and the electronic component of thermal conductivity, respectively. This is weighted by the spectral conductivity Σ^{crt} under the assumption of a constant relaxation time [i.e., Eq. (S11) with $\tau = 1$] to give

$$w_n^{\Sigma^{\text{crt}}}(\varepsilon) = |w_n(\varepsilon)| \cdot \Sigma^{\text{crt}}(\varepsilon). \quad (\text{S18})$$

Finally, we compute the normalized cumulative integral of the weights according to

$$w_n^{\text{cum}}(\varepsilon) = \frac{\int_{-\infty}^{\varepsilon} w_n^{\Sigma^{\text{crt}}}(\varepsilon') d\varepsilon'}{\int w_n^{\Sigma^{\text{crt}}}(\varepsilon') d\varepsilon'}. \quad (\text{S19})$$

We can then define a tuneable parameter λ than controls the minimum and maximum energy ranges within which to calculate the scattering rates. Namely,

$$\varepsilon_n^{\min} = \arg \min_{\varepsilon} \left| w_n^{\text{cum}}(\varepsilon) - \frac{\lambda}{2} \right|, \quad (\text{S20})$$

$$\varepsilon_n^{\max} = \arg \min_{\varepsilon} \left| w_n^{\text{cum}}(\varepsilon) - \left[1 - \frac{\lambda}{2} \right] \right|, \quad (\text{S21})$$

where λ can vary between 0 (in which case ε_n^{\min} and ε_n^{\max} will be the minimum and maximum energies in the band

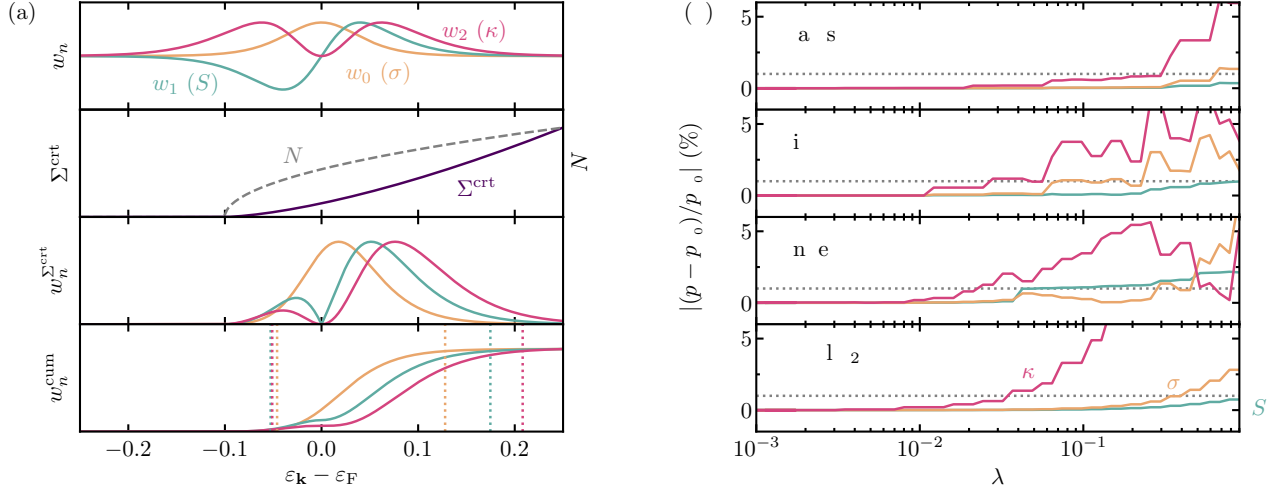


FIG. S2. (a) Procedure for obtaining the energy range in which to calculate scattering rates. The momentum coefficient weight w_n for $n = 0, 1, 2$ (top panel) is scaled by the spectral conductivity Σ^{crt} to give $w_n^{\Sigma^{\text{crt}}}$. The cumulative integral of the moment weights w_n^{cum} is used to determine the energy cutoffs (bottom panel). The dashed orange, teal, and pink lines give $\varepsilon_n^{\text{min}}$ and $\varepsilon_n^{\text{max}}$ for $n = 0, 1, 2$, respectively at $\lambda = 0.05$. The final values of ε^{min} and ε^{max} are taken as the smallest $\varepsilon_n^{\text{min}}$ and largest $\varepsilon_n^{\text{max}}$ values across all moments, respectively. (b) Convergence of electronic transport properties p as a function of λ at 300 K for GaAs, Si, SnSe, and CuAlO₂. Absolute percentage difference from converged value $|(p - p_{\lambda_0})/p_{\lambda_0}|$ given for conductivity ($p = \sigma$, orange), Seebeck coefficient (S , teal), and electronic contribution to the thermal conductivity (κ , pink), respectively. p_{λ_0} corresponds to the value of the transport properties at $\lambda = 0$ — i.e., the scattering rates for all \mathbf{k} -points are calculated explicitly. Convergence within 1 % is highlighted by a dashed gray line.

structure) and 1 (where $\varepsilon_n^{\text{min}}$ and $\varepsilon_n^{\text{max}}$ will be the same value). A value of $\lambda = 0.1$, indicates that 90 % of the integrated $w_n^{\Sigma^{\text{crt}}}$ will be included in the energy range. Alternatively put, a value of $\lambda = 0.1$ results in $\varepsilon_n^{\text{min}}$ and $\varepsilon_n^{\text{max}}$ taking the energies where $w_n^{\text{cum}} = 0.05$ and 0.95, respectively. The final energy range is given by $\varepsilon^{\text{min}} = \min(\{\varepsilon_n^{\text{min}} : n = 0, 1, 2\})$ and $\varepsilon^{\text{max}} = \max(\{\varepsilon_n^{\text{max}} : n = 0, 1, 2\})$. The scattering rate is only calculated for states where $\varepsilon^{\text{min}} \leq \varepsilon_{n\mathbf{k}} \leq \varepsilon^{\text{max}}$, with the scattering rates of the remaining states set to the average value of the rates that have been calculated explicitly. By setting λ to an appropriate value, the scattering rates for \mathbf{k} -points outside the energy range will not impact the transport properties.

To demonstrate the impact of λ and determine reasonable values to use in our calculations, we have investigated the convergence of the transport properties for GaAs, Si, SnSe, and CuAlO₂ at 300 K [Fig. S2(b)]. The conductivity, Seebeck coefficient, and electronic contribution to the thermal conductivity of all materials are converged to within than 1 % by $\lambda = 0.02$. In most cases, the Seebeck coefficient converges the fastest, most likely due to its weaker dependence on the scattering rate. The electronic contribution to the thermal conductivity is the slowest property to converge, as expected from its reliance on a broader momentum coefficient weight. If only the conductivity or Seebeck coefficient are of interest, a much larger value of λ can be used. For example, using a λ of 0.1 converges these properties to within 1 %. In our calculations, we employ a λ of 0.05 which offers

a reasonable trade-off between speed and convergence. This property is controlled in our software implementation through the `fd_tol` parameter.

C. Software implementation

An open-source implementation of the formalism, used to perform all calculations in this work, is released as a package called AMSET [33]. AMSET is freely available under a modified Berkeley Software Distribution (BSD) license. The current version is developed and maintained using Git and is accessible at <https://hackingmaterials.lbl.gov/amset>. The code can be run on both high-performance computing clusters or personal computers. AMSET is implemented in Python 3 and relies on several open-source libraries including pymatgen [34] for parsing VASP calculation outputs, BOLTZTRAP2 [20, 35] for Fourier interpolation of electronic eigenvalues and group velocities, SPGLIB [36] for symmetry analysis, QUADPY [31] for numerical integration, and MATPLOTLIB [37] for plotting. The NUMPY [38] and SCIPY [39] libraries are used extensively to minimize the cost of expensive matrix operations. All-electron wave function coefficients are generated from the pseudo-wave functions using the `MomentumMatrix` functionality of the PAWPY-SEED package [40].

AMSET can be used through either the the command-line or a Python application programming interface (API). A typical workflow, showing computational inputs

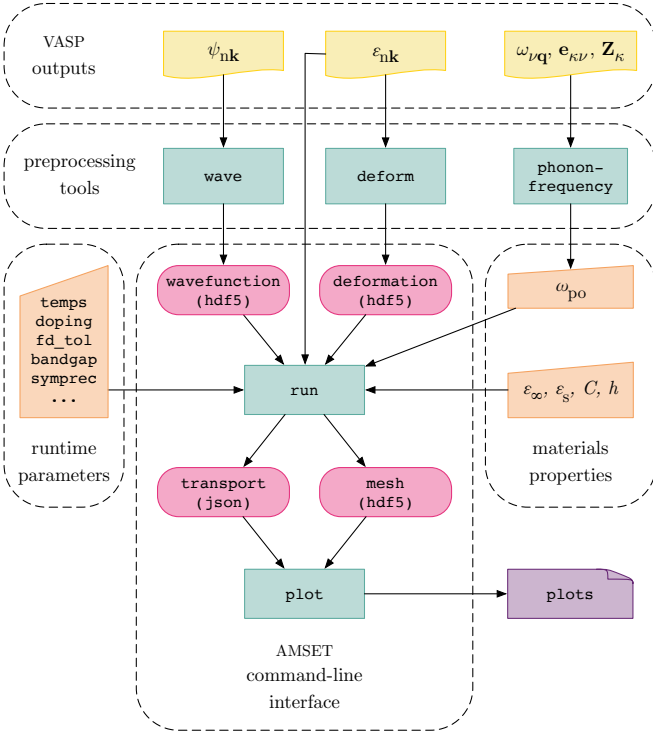


FIG. S3. Schematic of the AMSET program indicating the typical inputs and outputs, command-line tools, and program flow.

and outputs, is illustrated in Fig. (S3). The primary inputs are `vasprun.xml` and `WAVECAR` VASP output files, calculated on a uniform \mathbf{k} -point mesh. Additional settings, such as the materials parameters used to calculate scattering, the doping concentrations and temperatures to consider, and accuracy settings such as `fd_tol`, can be specified in a separate file or as command-line arguments. Information on all the available settings is provided on the AMSET website. After obtaining the first principles inputs, two pre-processing steps are required. Firstly, the all-electron wave function coefficients must be extracted from the VASP `WAVECAR` file using the `wave` tool. Secondly, the “effective-phonon-frequency” should be calculated from phonon frequencies and eigenvectors, and the Born effective charges using the `phonon-frequency` tool. This process is described in more detail in Section III A. Scattering rates and transport properties are computed using the `run` command. The primary output is the `transport` file, which by default contains the calculated mobility, Seebeck coefficient, and electronic contribution to the thermal conductivity in the JavaScript Object Notation (JSON) format. The scattering rates, and interpolated eigenvalues and group velocities can be written to the `mesh` file with the Hierarchical Data Format version 5 (HDF5) format [41] using the `write_mesh` option. Finally, the `plot` command can be used to plot transport properties, lifetimes, and electron linewidths from the `transport` and `mesh` files. The sumo package is used for plotting band structures [42].

D. Timing analysis

A primary goal of the present approach is to be amenable to high-throughput computational workflows. To investigate the computational requirements of the AMSET package, we have illustrated the time taken to calculate the scattering rates of several of the test materials in Fig. S4(a). All calculations were performed on a MacBook Pro with a quad core 2.9 GHz Intel Core i7 processor. The maximum time taken was 42 min for GaN, with most of the remaining materials completed in under 20 min. To understand which portions of the code are the most computationally demanding, we have broken down the results into the time taken to: (i) perform Fourier interpolation of electronic eigenvalues, (ii) compute the density of states through the tetrahedron method, (iii) obtain the scattering rates, (iv) calculate transport properties, and (v) write the output data to disk. We note, the benchmarks were performed with the `write_mesh` option enabled, so the output includes the scattering rates and interpolated band structure. In general, writing the output data takes the least amount of time relative to the other functions of the code. The breakdown for the rest of the computational steps depends strongly on the material and run time parameters, with most of the time spent calculating the scattering rates or transport properties.

To understand the scaling performance of AMSET with interpolation density, we have investigated the correlation of runtime with number of \mathbf{k} -points. We find there is not a simple correlation between the total number of \mathbf{k} -points and total runtime. Instead, each function of the code shows different scaling behaviour. The interpolation routines show $\mathcal{O}(n \log n)$ scaling (where n is the total number of \mathbf{k} -points in the dense mesh), which is consistent with the time complexity of the fast Fourier transform algorithm. The time taken to compute scattering does not correlate well with total number of \mathbf{k} -points. This is primarily as we only compute the scattering rates for the \mathbf{k} -points which fall within the energy cutoffs defined by the λ parameter (see Section II B). In addition, we use the symmetry of the reciprocal lattice to limit our calculations to the \mathbf{k} -points in the irreducible Brillouin zone (denoted \mathbf{k}^{ir} -points). The timing of the scattering routines correlates with the number of irreducible \mathbf{k} -points that fall within the energy cutoffs, exhibiting a $\mathcal{O}(n^{1.3})$ scaling complexity. We note that, while the scattering rate is only calculated for the irreducible \mathbf{k} -points within the energy cutoffs, the scattering rate for each state requires integrating the partial decay rates over the full Brillouin zone and not just the irreducible part. The time taken to compute transport properties correlates to the number the number of irreducible \mathbf{k} -points multiplied by the number of carrier concentrations and temperatures included in the calculation, with a $\mathcal{O}(n^{0.9})$ scaling complexity. The primary expense when computing transport properties is generating the energy-dependent tetrahedron integration weights used to obtain the spec-

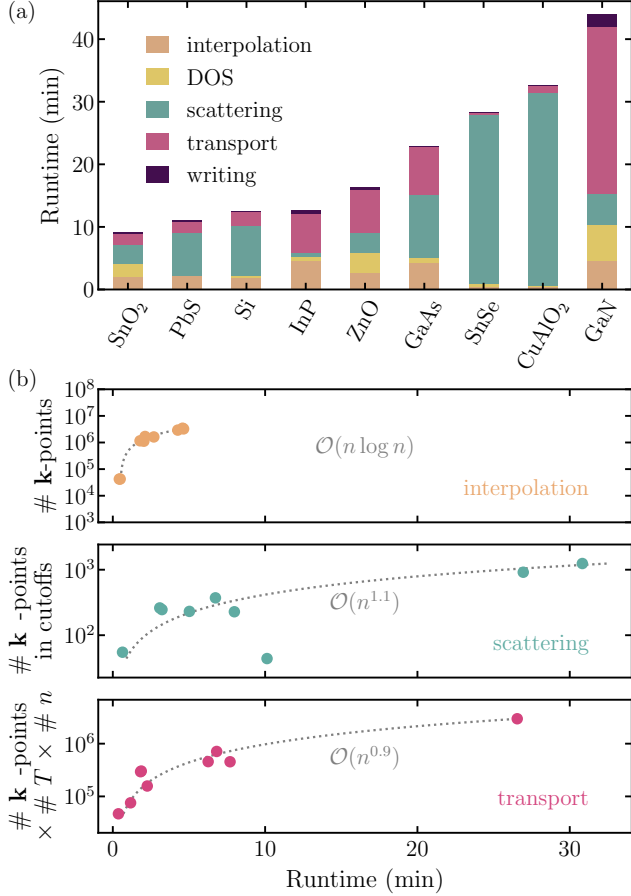


FIG. S4. Timing analysis for running AMSET on a selection of materials in the test set. Calculations performed using the materials parameters in Table IV and at the carrier concentrations and temperatures specified in Table VI. (a) The total runtime for each system, broken up into the different functions of the code. (b) Correlation between time and number (denoted by #) of \mathbf{k} -points for the interpolation, scattering, and transport routines. \mathbf{k}^{ir} indicates the \mathbf{k} -points within the irreducible Brillouin zone. The number of temperatures and carrier concentrations are denoted by $\# T$ and $\# n$, respectively. The computational complexity, provided in big O notation relative to the x-axis, is given in grey text and highlighted by dashed grey lines.

tral conductivity.

The total time to obtain transport properties is dominated by the calculation of the first-principles inputs (materials parameters and band structure calculation). In Table II, we provide the full timing information (in core hours) required to calculate all materials parameters used in this work. In Fig. (1) in the main text, we compare these times against DFPT+Wannier calculations performed using QUANTUM ESPRESSO and EPW. In Table III we provide the full breakdown of the DFPT+Wannier calculations, including the references from which the timing information and mobility was extracted.

TABLE II. Time required to obtain first-principles inputs given in core hours. Calculations were performed as described in the Computational Methodology. We note that the DFPT calculation listed here is performed only for a single \mathbf{q} -point at Γ and is used to obtain the effective phonon frequency, static and high-frequency dielectric constants, and piezoelectric constants rather than the matrix elements $g(\mathbf{k}, \mathbf{q})$. Static+NSCF (non self-consistent field) refers to a single point calculation on the relatively dense DFT \mathbf{k} -point meshes listed in Table V. Deformation and elastic refer to the total time required to calculate the deformation potential and elastic tensors

Material	Static+NSCF	Deformation	DFPT	Elastic	Total
GaAs	0.30	0.91	9.33	10.31	20.85
GaN	1.75	15.76	13.82	32.68	64.01
InP	0.55	4.91	9.01	4.48	18.94
ZnS	1.46	13.11	7.11	10.21	31.88
ZnSe	1.47	13.19	7.90	10.24	32.79
CdS	1.16	10.40	14.88	18.80	45.24
CdSe	1.12	10.07	16.61	17.28	45.08
CdTe	0.93	8.33	8.11	5.84	23.22
GaP	1.48	13.36	8.43	10.24	33.52
MAPbI ₃ ^a	6.67	40.03	901.12	65.03	1012.85
SiC	2.57	23.16	3.23	17.69	46.66
PbS	0.53	4.80	7.31	3.67	16.31
SnO ₂	1.34	12.03	14.11	18.08	45.56
ZnO	1.77	15.92	11.79	31.64	61.12
SnSe	1.90	17.14	48.48	24.00	91.53
CuAlO ₂	1.88	16.93	25.60	34.07	78.49
Si	2.65	7.96	2.62	8.78	22.01
Ba ₂ BiAu	1.78	16.05	9.16	5.55	32.49
NbFeSb	1.21	12.15	5.52	6.15	25.04

^a MA = CH₃NH₃

TABLE III. Time required to obtain electron mobility using DFPT+Wannier, as implemented in QUANTUM ESPRESSO (DFPT to obtain $g(\mathbf{k}, \mathbf{q})$ portion) and EPW (Wannier interpolation and scattering portion) in core hours. References are given to the publications in which the timing information and mobility results are reported

Material	DFPT	Scattering	Total	Refs.
Ba ₂ BiAu	7000	2500	9500	[43]
NbFeSb	4600	2600	7200	[44, 45]

E. Reproducing the Brooks–Herring model of impurity scattering

A primary advantage of the present approach is that it allows, for the first time, evaluation of ionized impurity scattering in anisotropic multi-band systems. Most modern computational evaluations of impurity scattering instead employ the closed-form Brooks–Herring formula [7, 8]. We will not reproduce the full derivation here but refer the reader to the excellent introduction provided in Ref. [46]. In this approach, the scattering matrix element

$$g_{nm}(\mathbf{k}, \mathbf{q}) = \frac{n_{\text{ii}}^{1/2} Z e}{\epsilon_s} \frac{1}{|\mathbf{q}|^2 + \beta^2}, \quad (\text{S22})$$

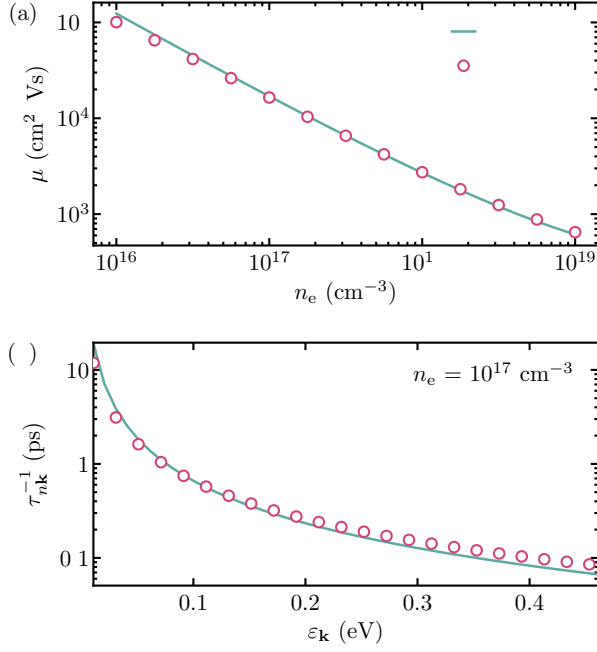


FIG. S5. Comparison of the (a) mobility and (b) carrier lifetime between AMSET and the analytical Brooks-Herring formulas for a parabolic band structure. Results calculated at a temperature of 500 K.

where n_{ii} and Z are the concentration and charge of the charge of the impurities, ϵ_s is the static dielectric constant, and β is the inverse screening length given by Eq. (S10), is analytically integrated for a single parabolic band [7, 8]. Under the assumption of complete overlap between the states the $n\mathbf{k}$ and $m\mathbf{k} + \mathbf{q}$, the resulting energy-dependent lifetime can be written

$$\tau_{BH}^{-1}(\epsilon) = \frac{n_{ii} Z^2 e^4 G(b)}{\pi 16 \sqrt{2} \sqrt{m_d^*} \epsilon_s^2} \epsilon^{-3/2}, \quad (S23)$$

where m_d^* is the density of states effective mass, ϵ_0 is the vacuum permittivity, $G(b) = \ln(b+1) - b/(b+1)$, and $b = 8m_d^* \epsilon / \hbar^2 \beta^2$. Further integration of the energy-dependent lifetime yields the well-known Brooks-Herring mobility formula

$$\mu_{BH} = \frac{128 \sqrt{2} \pi \epsilon_s^2 (k_B T)^{3/2}}{e^3 Z^2 \sqrt{m_d^*} n_{ii} G(b)}. \quad (S24)$$

To validate our implementation of ionized impurity scattering, we have generated a model parabolic electronic structure according to

$$\epsilon_{\mathbf{k}} = \frac{\hbar^2 |\mathbf{k}|^2}{2m_d^*}, \quad (S25)$$

$$\mathbf{v}_{\mathbf{k}} = \frac{\hbar |\mathbf{k}|}{m_d^*}, \quad (S26)$$

where $\epsilon_{\mathbf{k}}$ and $\mathbf{v}_{\mathbf{k}}$ are the energy and group velocity at wave vector \mathbf{k} , respectively. We calculated the ionized

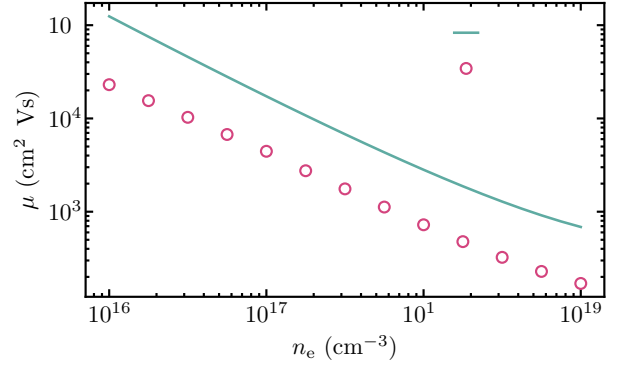


FIG. S6. Comparison of the electron mobility between AMSET and the analytical Brooks-Herring formulas for a parameterized Silicon-like band structure. Results calculated at a temperature of 500 K.

impurity scattering rate and resulting mobility using the AMSET package and Brooks-Herring formulas, parameterized according to $Z = 1$, $m_d^* = 0.2 m_0$, $\epsilon_s = 20 \epsilon_0$, $n_{ii} = 1 \times 10^{16} \text{ cm}^{-3}$ to $1 \times 10^{19} \text{ cm}^{-3}$, and $T = 500 \text{ K}$. A comparison between the two approaches is presented in Fig. (S5). Close agreement is observed for the both the mobility and carrier lifetime, indicating our approach is accurately reproducing the Brooks-Herring results.

The Brooks-Herring formula is known to lead to inaccurate results for non-parabolic band structures or systems with multiple valleys. To demonstrate this, we compare our method against Brooks-Herring on an idealized Silicon band structure, as parameterized in Refs. [47] and [48] and using the experimental effective masses according to

$$\epsilon_{\mathbf{k}} = \frac{\hbar^2 (k_x - k_{0,x})^2}{2m_{\parallel}^*} + \frac{\hbar^2 (k_y - k_{0,y})^2}{2m_{\perp}^*} + \frac{\hbar^2 (k_z - k_{0,z})^2}{2m_{\perp}^*}, \quad (S27)$$

where $m_{\parallel}^* = 0.98 m_0$, $m_{\perp}^* = 0.19 m_0$, and \mathbf{k}_0 denotes the wave vectors of the conduction band minima. The Brooks-Herring mobility is calculated using the harmonic mean of the effective masses, namely $3/(m_{\parallel}^{-1,*} + 2m_{\perp}^{-1,*}) = 0.26 m_0$. As can be seen in Fig. (S6), the Brooks-Herring mobility is considerably over estimated by almost an order of magnitude relative to the mobility computed by AMSET. This agrees well with empirical investigations into the mobility of Silicon that have noted the overestimation of the Brooks-Herring result [49].

TABLE IV. Materials parameters used to compute scatterings rates. \mathbf{C} is the elastic tensor in Voigt notation, with the unit GPa. ϵ_s and ϵ_∞ are the static and high-frequency dielectric constants in ϵ_0 . \mathbf{D}^{vb} and \mathbf{D}^{cb} are the absolute deformation potentials at the valence and conduction band edge, respectively. d is the dimensionless piezoelectric coefficient. ω_{po} is the effective polar phonon frequency given in THz. For all tensor properties, components that are not explicitly listed are zero

Material	C_{11}	C_{22}	C_{33}	C_{44}	C_{55}	C_{66}	C_{12}	C_{13}	C_{23}	$\epsilon_{s,11}$	$\epsilon_{s,22}$	$\epsilon_{s,33}$	$\epsilon_{\infty,11}$	$\epsilon_{\infty,22}$	$\epsilon_{\infty,33}$	D_{11}^{vb}	D_{22}^{vb}	D_{33}^{vb}	D_{11}^{cb}	D_{22}^{cb}	D_{33}^{cb}	d	ω_{po}
GaAs	99	99	99	51	51	51	41	41	41	10.3	10.3	10.3	12.2	12.2	12.2	1.2	1.2	1.2	8.6	8.6	8.6	0.0	8.2
GaN	325	325	358	90	90	107	112	78	78	5.9	5.9	6.1	10.5	10.5	11.7	8.2	8.2	8.5	15.0	15.0	15.2	0.0	19.0
InP	87	87	87	42	42	42	46	46	46	13.2	13.2	13.2	16.5	16.5	16.5	1.6	1.6	1.6	5.7	5.7	5.7	0.0	10.3
ZnS	96	96	96	46	46	46	55	55	55	5.9	5.9	5.9	9.4	9.4	9.4	0.5	0.5	0.5	7.0	7.0	7.0	0.1	7.9
ZnSe	82	82	82	37	37	37	47	47	47	7.3	7.3	7.3	10.7	10.7	10.7	0.8	0.8	0.8	5.7	5.7	5.7	0.0	5.9
CdS	80	80	85	15	15	17	45	37	37	6.0	6.0	6.1	9.8	9.8	10.4	0.3	0.3	0.8	2.4	2.4	3.2	0.2	6.5
CdSe	66	66	72	13	13	15	36	31	31	8.8	8.8	8.7	12.4	12.4	13.0	0.2	0.2	0.6	2.4	2.4	2.9	0.1	4.7
CdTe	47	47	47	19	19	19	30	30	30	9.3	9.3	9.3	12.8	12.8	12.8	0.1	0.1	0.1	2.9	2.9	2.9	0.0	3.9
GaP	125	125	125	65	65	65	52	52	52	10.6	10.6	10.6	12.9	12.9	12.9	0.4	0.4	0.4	13.0	13.0	13.0	0.0	10.3
MAPbI ₃ ^a	43	55	53	10	20	11	33	31	17	31.7	97.5	66.7	5.1	5.2	5.1	4.0	4.7	4.0	2.8	3.1	2.5	0.0	2.6
SiC	382	382	382	241	241	241	126	126	126	7.0	7.0	7.0	10.3	10.3	10.3	5.6	5.6	5.6	3.4	3.4	3.4	0.2	23.2
PbS	121	121	121	20	20	20	18	18	18	15.6	15.6	15.6	277.7	277.7	277.7	1.6	1.6	1.6	1.0	1.0	1.0	0.0	6.6
SnO ₂	376	215	215	178	84	84	127	127	136	4.9	4.6	4.6	10.5	13.6	13.6	0.9	1.5	1.5	10.7	13.2	13.2	0.0	10.4
ZnO	188	188	205	37	37	39	109	92	92	3.8	3.8	3.8	10.5	10.5	11.4	7.6	7.6	8.2	9.1	9.1	9.5	0.0	11.2
SnSe	30	39	67	12	28	14	13	28	8	16.9	15.3	18.7	32.3	27.1	46.3	13.8	15.9	14.7	11.2	9.8	14.5	0.0	3.2
CuAlO ₂	294	294	509	39	39	102	90	103	103	6.1	6.1	4.6	10.8	10.8	7.3	2.5	2.5	4.8	7.1	7.1	10.2	0.0	14.0
Si	144	144	144	75	75	75	53	53	53	13.0	13.0	13.0	13.0	13.0	13.0	6.5	1.1	1.1	8.1	0.5	0.5	0.0	0.0
Ba ₂ BiAu	69	69	69	17	17	17	18	18	18	37.2	37.2	37.2	22.2	22.2	22.2	3.0	3.0	3.0	2.9	2.9	2.9	0.0	1.8
NbFeSb	309	309	309	67	67	67	95	95	95	44.7	44.7	44.7	24.7	24.7	24.7	1.1	1.1	1.1	0.6	1.6	1.6	0.0	7.4

^a MA = CH₃NH₃

III. FIRST-PRINCIPLES INPUTS

A. Computational methodology

First-principles calculations were performed using Kohn-Sham DFT [50, 51] as implemented in the Vienna *ab initio* Simulation Package (VASP) [52–54]. All *ab initio* inputs were computed within the generalized-gradient approximation (GGA) [55] using the Perdew-Burke-Ernzerhof (PBE) exchange–correlation functional [56]. Calculations were performed in a plane-wave basis set with scalar relativistic pseudopotentials and with the interactions between core and valence electrons described using the projector augmented-wave method (PAW) [57, 58]. The set-up, submission, and management of first-principles calculations was handled using the ATOMATE workflow management software with the default parameters of version 0.8.3 [59, 60]. The plane-wave energy cutoff was set to 520 eV. Structure optimization was performed using the standard pymatgen `MPRelaxSet` with a reciprocal \mathbf{k} -point density of 64 \mathbf{k} -points/Å³ [34]. The uniform non-self-consistent calculations used as input to the scattering calculations were run with a reciprocal \mathbf{k} -point density of 1000 \mathbf{k} -points/Å³. Spin–orbit interactions were included for calculations on CH₃NH₃PbI₃ as they were necessary to obtain the correct band ordering at the conduction band minimum.

Piezoelectric constants, and static and high-frequency dielectric constants were computed using density functional perturbation theory (DFPT) based on the method developed and by Baroni and Resta [61] and adapted

to the PAW formalism by Gajdoš *et al.* [62]. Elastic constants were obtained through the stress-strain approach detailed in Ref. [63]. These calculations were automated using the `piezoelectric_constant`, `dielectric_constant`, and `elastic_constant` preset workflows available in ATOMATE [59].

Absolute volume deformation potentials were calculated in the manner proposed by Wei and Zunger [64]. The deformation potential describes the change in energy of the bands with change in volume and was calculated as $\mathbf{D}_{\mathbf{nk}} = \delta \epsilon_{\mathbf{nk}} / \delta S_{\alpha\beta}$ where \mathbf{S} is the uniform stress tensor. We average the deformation potential over contraction (−0.5%) and expansion (+0.5%) of the lattice. Furthermore, we calculate the full deformation potential tensor by computing the deformation for each component of the strain tensor. To account for shifts in the average electrostatic potential between deformed cells, we align the eigenvalues to the energy level of the deepest core state [64]. We note that, in practice, even the reference energy levels can shift upon strain, leading to a small degree of error in the deformation potentials for non-covalent crystals [65, 66].

The “effective phonon frequency” used in the calculation of polar-optical phonon scattering was determined from the phonon frequencies $\omega_{\mathbf{q}\nu}$ (where ν is a phonon branch and \mathbf{q} is a phonon wave vector) and eigenvectors $\mathbf{e}_{\kappa\nu}(\mathbf{q})$ (where κ is an atom in the unit cell). In order to capture scattering from the full phonon band structure in a single phonon frequency, each phonon mode is

weighted by the dipole moment it produces according to

$$w_\nu = \sum_{\kappa} \left[\frac{1}{M_{\kappa} \omega_{\mathbf{q}\nu}} \right]^{1/2} \times [\mathbf{q} \cdot \mathbf{Z}_{\kappa}^* \cdot \mathbf{e}_{\kappa\nu}(\mathbf{q})] \quad (\text{S28})$$

where \mathbf{Z}_{κ}^* is the Born effective charge. This naturally suppresses the contributions from transverse-optical and acoustic modes in the same manner as the more general formalism for computing Frölich based electron-phonon coupling [67, 68]. The weight is calculated only for Γ -point phonon frequencies and averaged over the unit sphere scaled by 0.01 to capture both the polar divergence at $\mathbf{q} \rightarrow 0$ and any anisotropy in the dipole moments. The effective phonon frequency is calculated as the weighted sum over all Γ -point phonon modes according to

$$\omega_{\text{po}} = \frac{\omega_{\Gamma\nu} w_\nu}{\sum_{\nu} w_\nu}. \quad (\text{S29})$$

We have released an open source tool **phonon-frequency** as part of the AMSET package that automates this computation from VASP calculation outputs.

B. Materials parameters

All materials parameters were computed from first-principles in the manner described in the Computational Methodology. A summary of the materials parameters used to compute carrier scattering rates is provided in Table IV. We have additionally employed the rigid scissor approximation such that band gaps match those calculated using the hybrid HSE06 exchange–correlation functional. Table V gives the band gaps and \mathbf{k} -point meshes employed in our calculations. Furthermore, we report the range of temperatures and carrier concentrations at which mobility and Seebeck coefficients are computed in Tables VI and VII.

C. Experimental data

In the main text, we calculate the mobility and Seebeck coefficient of 17 semiconductors and compare our results to experimental measurements. Our set of test materials spans a range of chemistries and doping-polarities and contains both isotropic and anisotropic materials. The set includes: (i) conventional semiconductors, Si, GaAs, GaN, GaP, InP, ZnS, ZnSe, CdS, CdSe, and SiC; (ii) the thermoelectric candidate SnSe; (iv) photovoltaic absorbers $\text{CH}_3\text{NH}_3\text{PbI}_3$, PbS, and CdTe; and (iii) transparent conductors, SnO_2 , ZnO, and CuAlO_2 . The reference samples are of the highest purity and crystallinity in order to minimize the mesoscopic effects of grain boundary scattering and crystallographic one-dimensional and two-dimensional defects (e.g., line dislocations, edge dislocations, and stacking faults). We favor bulk crystals over thin films (which can exhibit surface effects

TABLE V. Band gaps and \mathbf{k} -point meshes used to compute scatterings rates. $\varepsilon_{\text{g}}^{\text{HSE}}$ and $\varepsilon_{\text{g}}^{\text{exp}}$ are the band gaps calculated using the HSE06 functional and taken from experiment, respectively, with the references given in square brackets. The coarse \mathbf{k} -point mesh of the electronic band structures computed using density functional theory (DFT) are compared to the dense mesh obtained through Fourier interpolation.

Material	$\varepsilon_{\text{g}}^{\text{HSE}}$ (eV)	$\varepsilon_{\text{g}}^{\text{exp}}$ (eV)	k-point mesh	
			DFT	Interpolated
GaAs	1.33 [69]	1.52 [70]	$17 \times 17 \times 17$	$143 \times 143 \times 143$
GaN	3.06 [71]	3.26 [70]	$20 \times 20 \times 12$	$183 \times 183 \times 97$
InP	1.48 [72]	1.42 [70]	$16 \times 16 \times 16$	$151 \times 151 \times 151$
ZnS	3.22 ^a	3.72 [73]	$18 \times 18 \times 18$	$133 \times 133 \times 133$
ZnSe	2.24 ^a	2.82 [74]	$17 \times 17 \times 17$	$99 \times 99 \times 99$
CdS	2.12 ^a	2.48 [75]	$15 \times 15 \times 9$	$87 \times 87 \times 47$
CdSe	1.46 ^a	1.73 [76]	$15 \times 15 \times 9$	$87 \times 87 \times 47$
CdTe	1.34 ^a	1.48 [77]	$15 \times 15 \times 15$	$89 \times 89 \times 89$
GaP	2.37 ^a	2.24 [78]	$18 \times 18 \times 18$	$105 \times 105 \times 105$
MAPbI ₃ ^b	2.43 ^a	1.63 [79]	$7 \times 4 \times 6$	$51 \times 33 \times 47$
SiC	2.35 ^a	2.36 [80]	$22 \times 22 \times 22$	$125 \times 125 \times 125$
PbS	0.84 [81]	0.37 [82]	$16 \times 16 \times 16$	$119 \times 119 \times 119$
SnO ₂	2.88 [83]	3.60 [84]	$19 \times 13 \times 13$	$135 \times 91 \times 91$
ZnO	2.55 [85]	3.37 [82]	$20 \times 20 \times 12$	$145 \times 145 \times 77$
SnSe	1.10 [86]	0.90 [87]	$13 \times 13 \times 5$	$51 \times 49 \times 17$
CuAlO ₂	3.52 [88]	2.97 [89]	$14 \times 14 \times 4$	$57 \times 57 \times 13$
Si	1.15 [85]	1.14 [82]	$18 \times 18 \times 18$	$105 \times 105 \times 105$
Ba ₂ BiAu	0.88 ^a	—	$11 \times 11 \times 11$	$41 \times 41 \times 41$
NbFeSb	1.26 ^a	0.51 [90]	$16 \times 16 \times 16$	$45 \times 45 \times 45$

^a This work.

^b MA = CH_3NH_3

that impact carrier transport, e.g., strain, oxidation, off-stoichiometries, and surface dipole moments), however, in some cases we use epitaxial single crystal films. We also favor undoped or dilutely doped crystals (to less than 0.5 % at.) to avoid the formation of secondary crystal phases and degenerate doping. Lastly, we favor studies that look at a wide range of carrier concentrations and/or temperatures (greater than 300K). In all cases, experimental mobility is measured via the DC Hall effect. A summary of the reference data used in the comparisons against carrier mobility and Seebeck coefficient are provided in Tables VI and VII.

TABLE VI. Summary of temperature and doping conditions used for computing electron mobility. References provided to Electron-Phonon Wannier (EPW) calculations and experimental measurements performed at the same doping and temperature conditions, which are used in the comparison of electron mobilities in the main text and Supplemental Material

Material	Doping	T (K)	n (cm^{-3})	Exp.	EPW
GaAs	n -type	200–1000	3.0×10^{13}	[18]	[91]
GaAs	p -type	300	3.0×10^{13} – 8.6×10^{19}	[92, 93]	—
GaN	n -type	150–500	3.0×10^{16} – 5.5×10^{16}	[94]	[95]
InP	n -type	150–700	1.5×10^{16}	[96]	—
ZnS	n -type	300–650	1.0×10^{16}	[97]	—
ZnSe	n -type	200–1300	4.0×10^{14} – 2.0×10^{15}	[98, 99]	—
CdS	n -type	100–400	5.0×10^{15}	[100]	—
CdSe	n -type	150–1300	1.0×10^{16} – 1.0×10^{18}	[101, 102]	—
CdTe	n -type	100–1200	5.4×10^{14} – 1.4×10^{17}	[103, 104]	—
CdTe	p -type	550–1000	1.4×10^{16} – 6.7×10^{16}	[104]	—
GaP	n -type	100–500	3.0×10^{16}	[105]	—
MAPbI ₃ ^a	n -type	100–350	1.0×10^{14}	[106, 107]	[108]
SiC	n -type	100–850	3.7×10^{15} – 2.5×10^{16}	[109]	[110]
PbS	n -type	300–750	3.6×10^{17}	[111]	—
SnO ₂	n -type	300–700	1.0×10^{17}	[112]	—
ZnO	n -type	300–1000	8.2×10^{16}	[113]	—
SnSe	p -type	300–600	3.0×10^{17}	[114]	[115]
CuAlO ₂	p -type	300–430	1.3×10^{17} – 7.4×10^{18}	[89]	—
Si	n -type	300	2.0×10^{14} – 4.4×10^{18}	[116]	[3]
Ba ₂ BiAu	n -type	300	1×10^{14}	[43]	—
NbFeSb	p -type	300	2×10^{20}	[44, 45]	—

^a MA = CH₃NH₃

TABLE VII. Summary of temperature and doping conditions used for computing Seebeck coefficient. References provided to experimental measurements performed at the same doping and temperature conditions, which are used in the comparison of Seebeck coefficients in the main text and Supplemental Material

Material	Doping	T (K)	n (cm^{-3})	Exp.
GaAs	n -type	400–750	3.5×10^{17}	[117]
GaAs	p -type	350–750	6.4×10^{19}	[118]
GaN	n -type	100–300	1.3×10^{19}	[119]
InP	n -type	150–700	2.1×10^{17}	[120]
CdS	n -type	130–300	2.8×10^{15}	[121]
PbS	n -type	300–800	2.5×10^{19}	[122]
SnO ₂	n -type	300–800	8.2×10^{18}	[123]
ZnO	n -type	200–1000	5.2×10^{17}	[124]
SnSe	p -type	300–600	3.0×10^{17}	[114]
Si	n -type	300	1×10^{14} – 1×10^{19}	[125, 126]

IV. MOBILITY RESULTS

A. Temperature and carrier dependent mobility

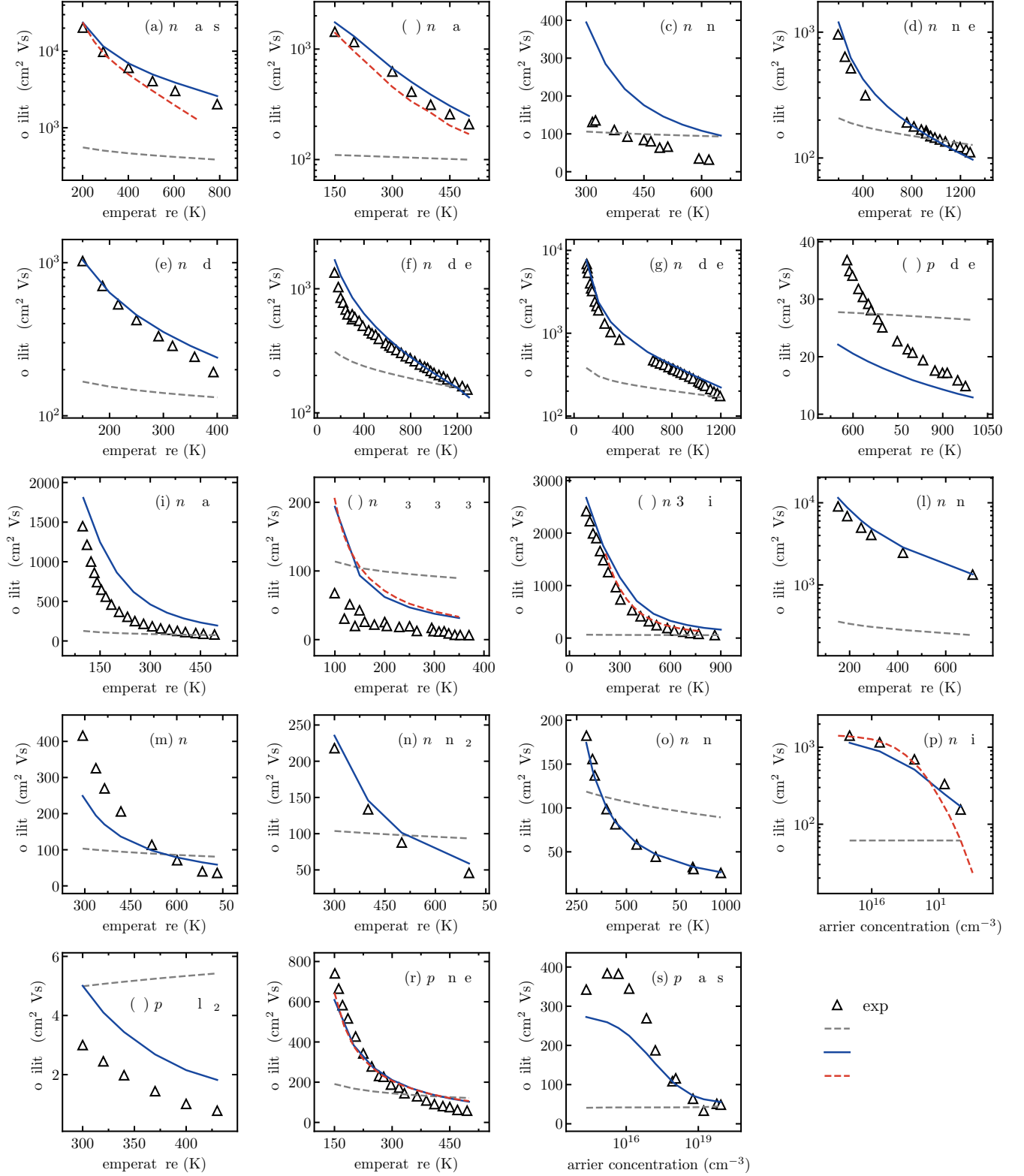


FIG. S7. Mobility against temperature or carrier-concentration for all test materials, computed using the HSE06 band gap.

B. Scattering limited mobilities

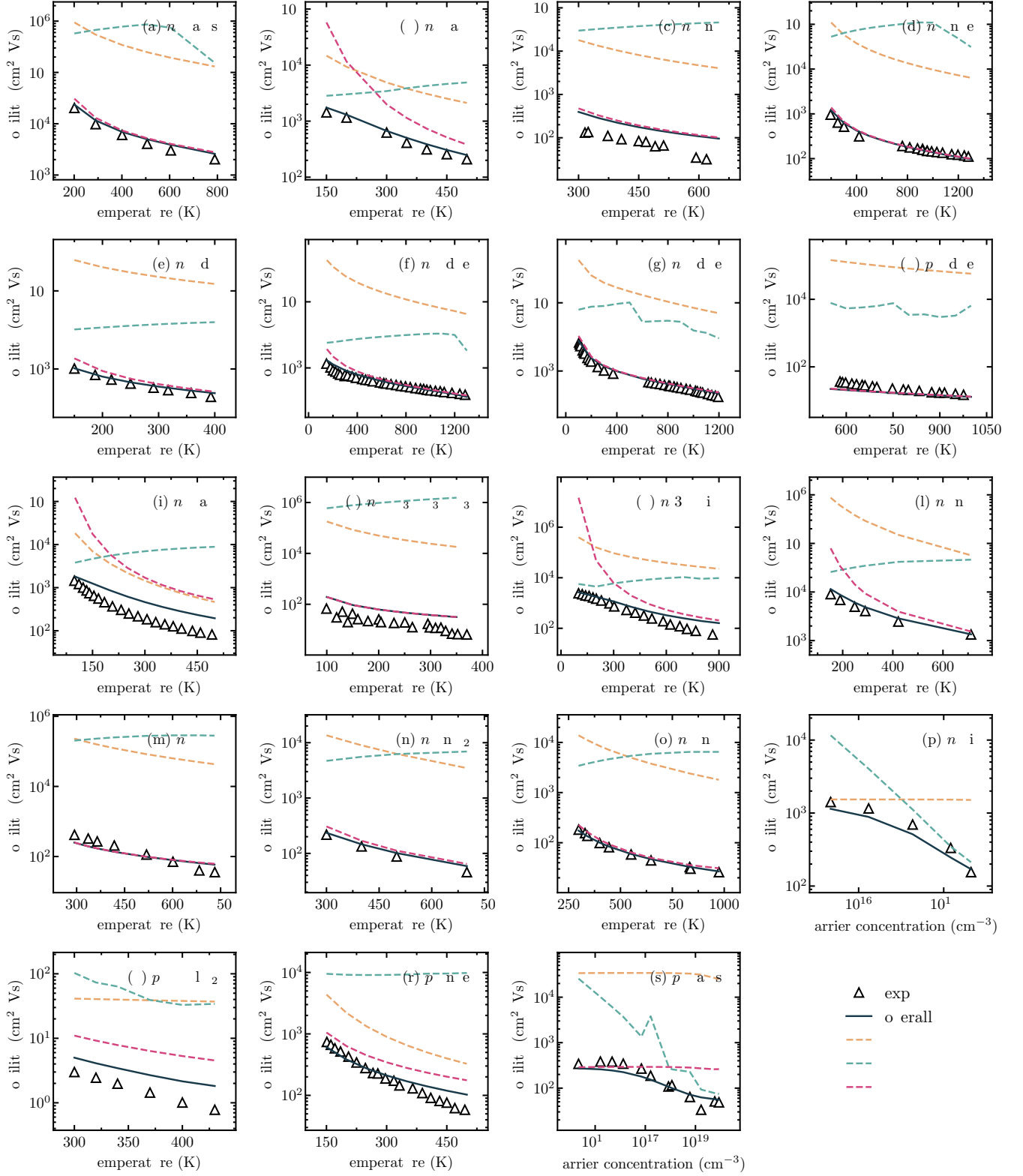


FIG. S8. Mobility limited by different scattering mechanisms against temperature or carrier-concentration for all test materials, computed using the HSE06 band gap.

V. SEEBECK COEFFICIENT RESULTS

A. Temperature- and carrier concentration-dependent Seebeck coefficient

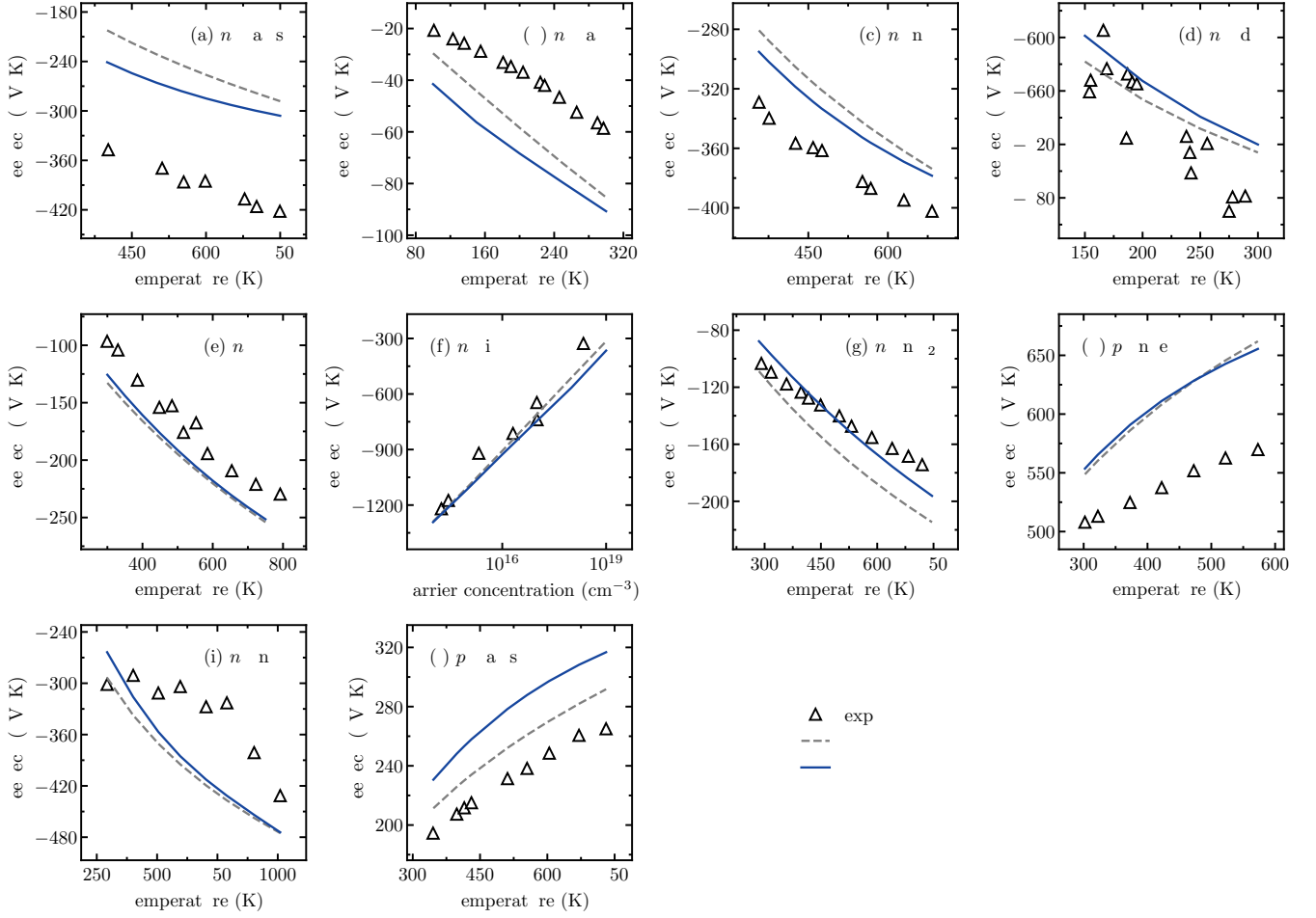


FIG. S10. Seebeck coefficient against temperature for all test materials, computed using the HSE06 band gap.

B. Seebeck coefficient calculated using the HSE06 functional

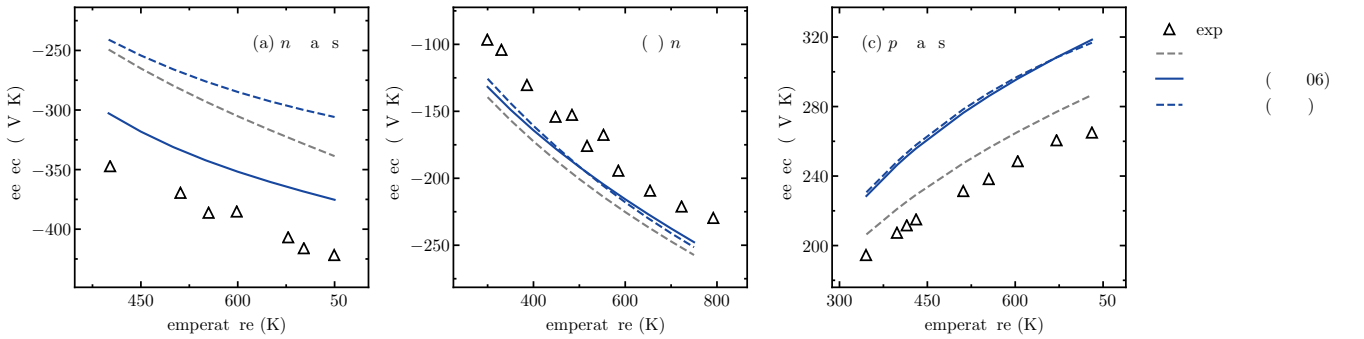


FIG. S11. Seebeck coefficient against temperature for a set of test materials computed using HSE06 electronic structures.

VI. SCATTERING RATE COMPARISON

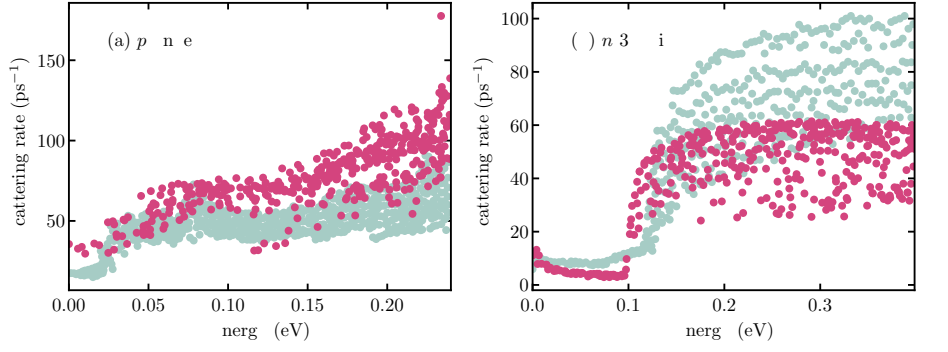


FIG. S12. Computed scattering rates compared against EPW calculations [3, 91, 110, 115]. Results calculated at 300 K using the the lowest carrier concentrations for each material given in Table. VI

VII. COMPARISON AGAINST CRT AND EPW

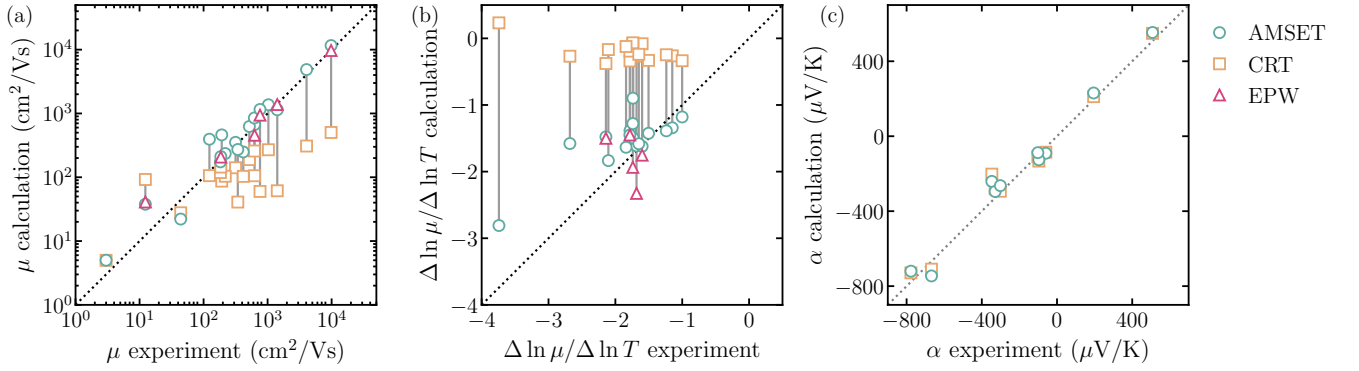


FIG. S13. Comparison between AMSET, constant relaxation time approximation calculations, EPW calculations, and experiments for (a) carrier mobilities at 300 K (b) the exponential temperature trend of carrier mobilities, and (c) Seebeck coefficients at 300 K.

VIII. BAND STRUCTURES

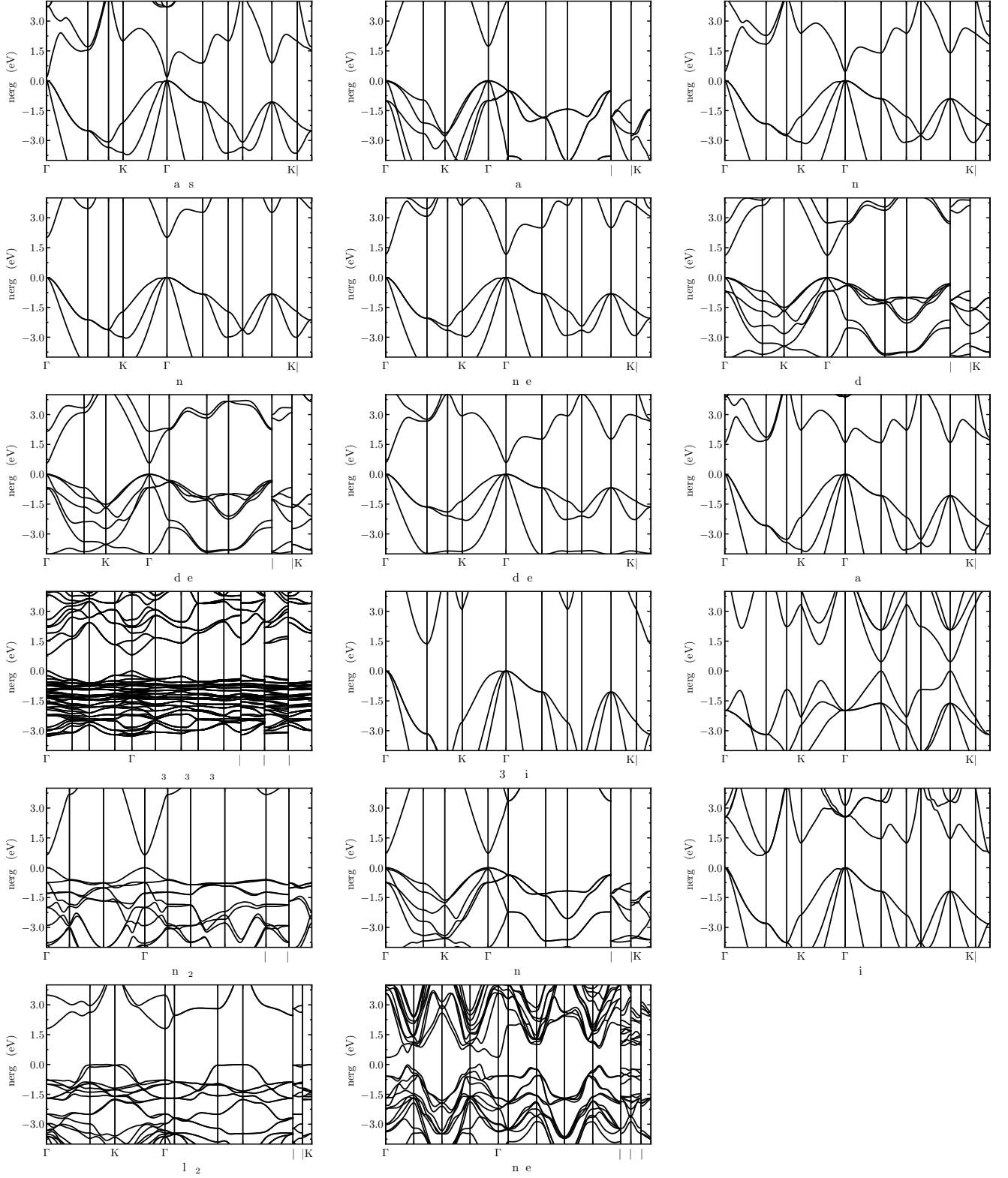


FIG. S14. Band structures (pre-scissor operation) calculated using the PBE exchange–correlation functional, interpolated from a uniform \mathbf{k} -point mesh using the BOLTZTRAP2 package.

-
- [1] J. Ziman, *Electrons and Phonons*, Oxford University Press (1960).
- [2] S. Poncé, W. Li, S. Reichardt, and F. Giustino, First-principles calculations of charge carrier mobility and conductivity in bulk semiconductors and two-dimensional materials, *Rep. Prog. Phys.* **83**, 036501 (2020).
- [3] S. Poncé, E. R. Margine, and F. Giustino, Towards predictive many-body calculations of phonon-limited carrier mobilities in semiconductors, *Phys. Rev. B* **97**, 121201 (2018).
- [4] W. Li, Electrical transport limited by electron-phonon coupling from Boltzmann transport equation: An *ab initio* study of Si, Al, and MoS₂, *Phys. Rev. B* **92**, 075405 (2015).
- [5] G. Grimvall, *The Electron-Phonon interaction in metals* (North-Holland, Amsterdam, 1981).
- [6] F. Giustino, M. L. Cohen, and S. G. Louie, Electron-phonon interaction using Wannier functions, *Phys. Rev. B* **76**, 165108 (2007).
- [7] H. Brooks, Scattering by ionized impurities in semiconductors, in *Phys. Rev.*, Vol. 83 (1951) pp. 879–879.
- [8] C. Herring and E. Vogt, Transport and deformation-potential theory for many-valley semiconductors with anisotropic scattering, *Phys. Rev.* **101**, 944 (1956).
- [9] J. Bardeen and W. Shockley, Deformation potentials and mobilities in non-polar crystals, *Phys. Rev.* **80**, 72 (1950).
- [10] F. S. Khan and P. B. Allen, Deformation potentials and electron-phonon scattering: Two new theorems, *Phys. Rev. B* **29**, 3341 (1984).
- [11] E. Kartheuser and S. Rodriguez, Deformation potentials and the electron-phonon interaction in metals, *Phys. Rev. B* **33**, 772 (1986).
- [12] R. Resta, Deformation-potential theorem in metals and in dielectrics, *Phys. Rev. B* **44**, 11035 (1991).
- [13] H. Meijer and D. Polder, Note on polar scattering of conduction electrons in regular crystals, *Physica* **19**, 255 (1953).
- [14] W. A. Harrison, Mobility in zinc blende and indium antimonide, *Phys. Rev.* **101**, 903 (1956).
- [15] D. Rode, Low-field electron transport, in *Semiconductors and semimetals*, Vol. 10 (Elsevier, 1975) pp. 1–89.
- [16] H. Fröhlich, Electrons in lattice fields, *Adv. Phys.* **3**, 325 (1954).
- [17] M. Born, Quantenmechanik der stoßvorgänge, *Z. Phys.* **38**, 803 (1926).
- [18] D. Rode and S. Knight, Electron transport in GaAs, *Phys. Rev. B* **3**, 2534 (1971).
- [19] L. Onsager, Reciprocal relations in irreversible processes. i., *Phys. Rev.* **37**, 405 (1931).
- [20] G. K. Madsen, J. Carrete, and M. J. Verstraete, BoltzTraP2, a program for interpolating band structures and calculating semi-classical transport coefficients, *Comput. Phys. Commun.* **231**, 140 (2018).
- [21] P. E. Blöchl, O. Jepsen, and O. K. Andersen, Improved tetrahedron method for Brillouin-zone integrations, *Phys. Rev. B* **49**, 16223 (1994).
- [22] G. K. Madsen, J. Carrete, and M. J. Verstraete, BoltzTraP2, a program for interpolating band structures and calculating semi-classical transport coefficients, *Comput. Phys. Commun.* **231**, 140 (2018).
- [23] G. K. Madsen and D. J. Singh, BoltzTraP. A code for calculating band-structure dependent quantities, *Comput. Phys. Commun.* **175**, 67 (2006).
- [24] R. N. Euwema, D. J. Stukel, T. C. Collins, J. S. Dewitt, and D. G. Shankland, Crystalline Interpolation with Applications to Brillouin-Zone Averages and Energy-Band Interpolation, *Phys. Rev.* **178**, 1419 (1969).
- [25] D. Koelling and J. Wood, On the interpolation of eigenvalues and a resultant integration scheme, *J. Comput. Phys.* **67**, 253 (1986).
- [26] D. G. Shankland, Fourier transformation by smooth interpolation, *Int. J. Quantum Chem.* **5**, 497 (2009).
- [27] W. E. Pickett, H. Krakauer, and P. B. Allen, Smooth Fourier interpolation of periodic functions, *Phys. Rev. B* **38**, 2721 (1988).
- [28] G. Lehmann and M. Taut, On the numerical calculation of the density of states and related properties, *Phys. Status Solidi B* **54**, 469 (1972).
- [29] H. Xiao and Z. Gimbutas, A numerical algorithm for the construction of efficient quadrature rules in two and higher dimensions, *Comput. Math. with Appl.* **59**, 663 (2010).
- [30] M. Festa and A. Sommariva, Computing almost minimal formulas on the square, *J. Comput. Appl. Math* **236**, 4296 (2012).
- [31] N. Schlömer, N. R. Papior, R. Zetter, M. Ancellin, and D. Arnold, *nschloe/quadpy v0.14.11* (2020).
- [32] C. Friedrich, Tetrahedron integration method for strongly varying functions: Application to the G T self-energy, *Phys. Rev. B* **100**, 075142 (2019).
- [33] A. Ganose, *AMSET: ab initio scattering and transport* (2020).
- [34] S. P. Ong, W. D. Richards, A. Jain, G. Hautier, M. Kocher, S. Cholia, D. Gunter, V. L. Chevrier, K. A. Persson, and G. Ceder, Python Materials Genomics (pymatgen): A robust, open-source python library for materials analysis, *Comput. Mater. Sci.* **68**, 314 (2013).
- [35] G. K. Madsen and D. J. Singh, BoltzTraP. a code for calculating band-structure dependent quantities, *Comput. Phys. Commun.* **175**, 67 (2006).
- [36] A. Togo and I. Tanaka, *Spglib: A software library for crystal symmetry search*, ArXiv180801590 Cond-Mat (2018), [arXiv:1808.01590 \[cond-mat\]](https://arxiv.org/abs/1808.01590).
- [37] J. D. Hunter, Matplotlib: A 2D Graphics Environment, *Comput. Sci. Eng.* **9**, 90 (2007).
- [38] S. Van Der Walt, S. C. Colbert, and G. Varoquaux, The NumPy array: A structure for efficient numerical computation, *Comput. Sci. Eng.* **13**, 22 (2011), [arXiv:1102.1523](https://arxiv.org/abs/1102.1523).
- [39] SciPy 1.0 Contributors, P. Virtanen, R. Gommers, T. E. Oliphant, M. Haberland, T. Reddy, D. Cournapeau, E. Burovski, P. Peterson, W. Weckesser, J. Bright, S. J. van der Walt, M. Brett, J. Wilson, K. J. Millman, N. Mayorov, A. R. J. Nelson, E. Jones, R. Kern, E. Larson, C. J. Carey, Í. Polat, Y. Feng, E. W. Moore, J. VanderPlas, D. Laxalde, J. Perktold, R. Cimrman, I. Henriksen, E. A. Quintero, C. R. Harris, A. M. Archibald, A. H. Ribeiro, F. Pedregosa, and P. van Mulbregt, SciPy 1.0: Fundamental algorithms for scientific computing in Python, *Nat. Methods* **17**, 261 (2020).

- [40] K. Bystrom, D. Broberg, S. Dwaraknath, K. A. Persson, and M. Asta, Pawpyseed: Perturbation-extrapolation band shifting corrections for point defect calculations, *ArXiv190411572 Cond-Mat* (2019), [arXiv:1904.11572 \[cond-mat\]](#).
- [41] M. Folk, G. Heber, Q. Koziol, E. Pourmal, and D. Robinson, An overview of the HDF5 technology suite and its applications, in *Proceedings of the EDBT/ICDT 2011 Workshop on Array Databases* (2011) pp. 36–47.
- [42] A. M. Ganose, A. J. Jackson, and D. O. Scanlon, sumo: Command-line tools for plotting and analysis of periodic *ab initio* calculations, *Journal of Open Source Software* **3**, 717 (2018).
- [43] J. Park, Y. Xia, and V. Ozoliņš, High Thermoelectric Power Factor and Efficiency from a Highly Dispersive Band in Ba_2BiAu , *Phys. Rev. Applied* **11**, 014058 (2019).
- [44] J. Zhou, H. Zhu, T.-H. Liu, Q. Song, R. He, J. Mao, Z. Liu, W. Ren, B. Liao, D. J. Singh, Z. Ren, and G. Chen, Large thermoelectric power factor from crystal symmetry-protected non-bonding orbital in half-Heuslers, *Nat. Commun.* **9**, 1721 (2018).
- [45] G. Samsonidze and B. Kozinsky, Accelerated screening of thermoelectric materials by first-principles computations of electron-phonon scattering, *Adv. Energy Mater.* **8**, 1800246 (2018).
- [46] D. Chattopadhyay and H. J. Queisser, Electron scattering by ionized impurities in semiconductors, *Rev. Mod. Phys.* **53**, 745 (1981).
- [47] G. Dresselhaus, A. F. Kip, and C. Kittel, Cyclotron Resonance of Electrons and Holes in Silicon and Germanium Crystals, *Phys. Rev.* **98**, 368 (1955).
- [48] P. Y. Yu and M. Cardona, *Fundamentals of semiconductors*, edited by H. E. Stanley and W. T. Rhodes (Springer, 2010).
- [49] P. Norton, T. Braggins, and H. Levinstein, Impurity and Lattice Scattering Parameters as Determined from Hall and Mobility Analysis in n-Type Silicon, *Phys. Rev. B* **8**, 5632 (1973).
- [50] P. Hohenberg and W. Kohn, Inhomogeneous Electron Gas, *Phys. Rev.* **136**, B864 (1964).
- [51] W. Kohn and L. J. Sham, Self-Consistent Equations Including Exchange and Correlation Effects, *Phys. Rev.* **140**, A1133 (1965).
- [52] G. Kresse and J. Hafner, Ab initio molecular-dynamics simulation of the liquid-metal-amorphous-semiconductor transition in germanium, *Phys. Rev. B* **49**, 14251 (1994).
- [53] G. Kresse and J. Furthmüller, Efficient iterative schemes for ab initio total-energy calculations using a plane-wave basis set, *Phys. Rev. B* **54**, 11169 (1996).
- [54] G. Kresse and J. Furthmüller, Efficiency of ab-initio total energy calculations for metals and semiconductors using a plane-wave basis set, *Comput. Mater. Sci.* **6**, 15 (1996).
- [55] J. P. Perdew and W. Yue, Accurate and simple density functional for the electronic exchange energy: Generalized gradient approximation, *Phys. Rev. B* **33**, 8800 (1986).
- [56] J. P. Perdew, K. Burke, and M. Ernzerhof, Generalized gradient approximation made simple, *Phys. Rev. Lett.* **77**, 3865 (1996).
- [57] P. E. Blöchl, Projector augmented-wave method, *Phys. Rev. B* **50**, 17953 (1994), [arXiv:1408.4701v2](#).
- [58] G. Kresse and D. Joubert, From ultrasoft pseudopotentials to the projector augmented-wave method, *Phys. Rev. B* **59**, 1758 (1999).
- [59] K. Mathew, J. H. Montoya, A. Faghaninia, S. Dwarakanath, M. Aykol, H. Tang, I. heng Chu, T. Smidt, B. Bocklund, M. Horton, J. Dagdelen, B. Wood, Z. K. Liu, J. Neaton, S. P. Ong, K. Persson, and A. Jain, Atomate: A high-level interface to generate, execute, and analyze computational materials science workflows, *Comput. Mater. Sci.* **139**, 140 (2017).
- [60] Atomate v0.8.3 (2018).
- [61] S. Baroni and R. Resta, *Ab Initio* calculation of the macroscopic dielectric constant in silicon, *Phys. Rev. B* **33**, 7017 (1986).
- [62] M. Gajdoš, K. Hummer, G. Kresse, J. Furthmüller, and F. Bechstedt, Linear optical properties in the projector-augmented wave methodology, *Phys. Rev. B* **73**, 045112 (2006), [arXiv:cond-mat/0510491](#).
- [63] M. de Jong, W. Chen, T. Angsten, A. Jain, R. Notestine, A. Gamst, M. Sluiter, C. Krishna Ande, S. van der Zwaag, J. J. Plata, C. Toher, S. Curtarolo, G. Ceder, K. A. Persson, and M. Asta, Charting the complete elastic properties of inorganic crystalline compounds, *Sci. Data* **2**, 150009 (2015).
- [64] S.-H. Wei and A. Zunger, Predicted band-gap pressure coefficients of all diamond and zinc-blende semiconductors: Chemical trends, *Phys. Rev. B* **60**, 5404 (1999).
- [65] R. Resta, L. Colombo, and S. Baroni, Absolute deformation potentials in semiconductors, *Phys. Rev. B* **41**, 12358 (1990).
- [66] Y.-H. Li, A. Walsh, S. Chen, W.-J. Yin, J.-H. Yang, J. Li, J. L. F. Da Silva, X. G. Gong, and S.-H. Wei, Revised *ab initio* natural band offsets of all group IV, II-VI, and III-V semiconductors, *Appl. Phys. Lett.* **94**, 212109 (2009).
- [67] C. Verdi and F. Giustino, Fröhlich electron-phonon vertex from first principles, *Phys. Rev. Lett.* **115**, 176401 (2015).
- [68] J. Sjakste, N. Vast, M. Calandra, and F. Mauri, Wannier interpolation of the electron-phonon matrix elements in polar semiconductors: Polar-optical coupling in GaAs, *Phys. Rev. B* **92**, 054307 (2015).
- [69] Y.-S. Kim, M. Marsman, G. Kresse, F. Tran, and P. Blaha, Towards efficient band structure and effective mass calculations for III-V direct band-gap semiconductors, *Phys. Rev. B* **82**, 205212 (2010).
- [70] I. Vurgaftman, J. R. Meyer, and L. R. Ram-Mohan, Band parameters for III-V compound semiconductors and their alloys, *J. Appl. Phys.* **89**, 5815 (2001).
- [71] A. Stroppa and G. Kresse, Unraveling the Jahn-Teller effect in Mn-doped GaN using the Heyd-Scuseria-Ernzerhof hybrid functional, *Phys. Rev. B* **79**, 201201 (2009).
- [72] Y.-S. Kim, K. Hummer, and G. Kresse, Accurate band structures and effective masses for InP, InAs, and InSb using hybrid functionals, *Phys. Rev. B* **80**, 035203 (2009).
- [73] T. K. Tran, W. Park, W. Tong, M. M. Kyi, B. K. Wagner, and C. J. Summers, Photoluminescence properties of ZnS epilayers, *J. Appl. Phys.* **81**, 2803 (1997).
- [74] A. Mang, K. Reimann, and S. Rübenacke, Two-photon spectroscopy in ZnSe under hydrostatic pressure, in *Proceedings of the 22nd International Conference on the*

- Physics of Semiconductors*, edited by D. J. Lockworth (World Scientific, Singapore, 1994) pp. 317–320.
- [75] S. Ninomiya and S. Adachi, Optical properties of wurtzite CdS, *J. Appl. Phys.* **78**, 1183 (1995).
 - [76] S. Ninomiya and S. Adachi, Optical properties of cubic and hexagonal CdSe, *J. Appl. Phys.* **78**, 4681 (1995).
 - [77] P. Lemasson, Free excitons at room temperature in cadmium telluride: A photoelectrochemical evidence, *Solid State Commun.* **43**, 627 (1982).
 - [78] L. M. Foster and M. Pilkuhn, Electroluminescence near band gap in gallium phosphide containing shallow donor and acceptor levels, *Appl. Phys. Lett.* **7**, 65 (1965).
 - [79] M. E. Ziffer, J. C. Mohammed, and D. S. Ginger, Electroabsorption spectroscopy measurements of the exciton binding energy, electron-hole reduced effective mass, and band gap in the perovskite $\text{CH}_3\text{NH}_3\text{PbI}_3$, *ACS Photonics* **3**, 1060 (2016).
 - [80] X. Liu, L. Li, Q. Li, Y. Li, and F. Lu, Optical and mechanical properties of C, Si, Ge, and 3C-SiC determined by first-principles theory using Heyd-Scuseria-Ernzerhof functional, *Mater. Sci. Semicond. Process* **16**, 1369 (2013).
 - [81] A. Walsh, Effects of reduced dimensionality on the electronic structure and defect chemistry of semiconducting hybrid organic-inorganic PbS solids, *Proc. R. Soc. A* **467**, 1970 (2011).
 - [82] O. Madelung, *Semiconductors: data handbook* (Springer Science & Business Media, 2012).
 - [83] F. Tran and P. Blaha, Importance of the Kinetic Energy Density for Band Gap Calculations in Solids with Density Functional Theory, *J. Phys. Chem. A* **121**, 3318 (2017).
 - [84] M. Batzill and U. Diebold, The surface and materials science of tin oxide, *Prog. Surf. Sci.* **79**, 47 (2005).
 - [85] Y. Hinuma, A. Grüneis, G. Kresse, and F. Oba, Band alignment of semiconductors from density-functional theory and many-body perturbation theory, *Phys. Rev. B* **90**, 155405 (2014).
 - [86] Y. Huang, C. Wang, X. Chen, D. Zhou, J. Du, S. Wang, and L. Ning, First-principles study on intrinsic defects of SnSe, *RSC Adv.* **7**, 27612 (2017).
 - [87] H. Soliman, D. Abdel Hady, K. Abdel Rahman, S. Youssef, and A. El-Shazly, Optical properties of tin-selenid films, *Physica A* **216**, 77 (1995).
 - [88] D. O. Scanlon and G. W. Watson, Conductivity Limits in CuAlO_2 from Screened-Hybrid Density Functional Theory, *J. Phys. Chem. Lett.* **1**, 3195 (2010).
 - [89] J. Tate, H. L. Ju, J. C. Moon, A. Zakutayev, A. P. Richard, J. Russell, and D. H. McIntyre, Origin of p-type conduction in single-crystal CuAlO_2 , *Phys. Rev. B* **80**, 165206 (2009).
 - [90] R. He, D. Kraemer, J. Mao, L. Zeng, Q. Jie, Y. Lan, C. Li, J. Shuai, H. S. Kim, Y. Liu, D. Broido, C.-W. Chu, G. Chen, and Z. Ren, Achieving high power factor and output power density in p-type half-Heuslers $\text{Nb}_{1-x}\text{Ti}_x\text{FeSb}$, *Proc. Natl. Acad. Sci.* **113**, 13576 (2016).
 - [91] J.-J. Zhou and M. Bernardi, *Ab Initio* electron mobility and polar phonon scattering in GaAs, *Phys. Rev. B* **94**, 201201 (2016).
 - [92] L. Janšák and T. S. Lagunova, Effect of magnetic field on the impurity conduction in p-GaAs, *Phys. Stat. Sol. (a)* **13**, K151 (1972).
 - [93] D. E. Hill, Activation Energy of Holes in Zn-Doped GaAs, *J. Appl. Phys.* **41**, 1815 (1970).
 - [94] D. Steigerwald, S. Rudaz, H. Liu, R. S. Kern, W. Götz, and R. Fletcher, III-V Nitride semiconductors for high-performance blue and green light-emitting devices, *JOM* **49**, 18 (1997).
 - [95] S. Poncé, D. Jena, and F. Giustino, Hole mobility of strained GaN from first principles, *Phys. Rev. B* **100**, 085204 (2019).
 - [96] V. V. Galavanov and N. V. Siukaev, On Mechanism of Electron Scattering in InP, *phys. stat. sol. (b)* **38**, 523 (1970).
 - [97] F. Kröger, Some optical and electrical measurements on blue fluorescent ZnS-Cl single crystals, *Physica* **22**, 637 (1956).
 - [98] M. Aven, High Electron Mobility in Zinc Selenide Through Low-Temperature Annealing, *J. Appl. Phys.* **42**, 1204 (1971).
 - [99] F. Smith, Evidence for a native donor in ZnSe from high temperature electrical measurements, *Solid State Commun.* **7**, 1757 (1969).
 - [100] B. Pödör, J. Balázs, and M. Hársy, Electron concentration and mobility in CdS single crystals, *phys. stat. sol. (a)* **8**, 613 (1971).
 - [101] R. A. Btirmeister and D. A. Stevenson, Electrical Properties of n-Type CdSe, *phys. stat. sol. (b)* **24**, 683 (1967).
 - [102] F. Smith, High temperature electrical properties of CdSe: Evidence for a native donor, *Solid State Commun.* **8**, 263 (1970).
 - [103] B. Segall, M. R. Lorenz, and R. E. Halsted, Electrical Properties of n-Type CdTe, *Phys. Rev.* **129**, 2471 (1963).
 - [104] F. T. J. Smith, Electrically active point defects in cadmium telluride, *Metall. Mater. Trans. B* **1**, 617 (1970).
 - [105] R. C. Taylor, J. F. Woods, and M. R. Lorenz, Electrical and Optical Properties of Vapor-Grown GaP, *J. Appl. Phys.* **39**, 5404 (1968).
 - [106] M. Karakus, S. A. Jensen, F. D'Angelo, D. Turchinovich, M. Bonn, and E. Cánovas, Phonon-Electron Scattering Limits Free Charge Mobility in Methylammonium Lead Iodide Perovskites, *J. Phys. Chem. Lett.* **6**, 4991 (2015).
 - [107] R. L. Milot, G. E. Eperon, H. J. Snaith, M. B. Johnston, and L. M. Herz, Temperature-Dependent Charge-Carrier Dynamics in $\text{CH}_3\text{NH}_3\text{PbI}_3$ Perovskite Thin Films, *Adv. Funct. Mater.* **25**, 6218 (2015).
 - [108] S. Poncé, M. Schlipf, and F. Giustino, Origin of Low Carrier Mobilities in Halide Perovskites, *ACS Energy Lett.* **4**, 456 (2019).
 - [109] M. Shinohara, M. Yamanaka, H. Daimon, E. Sakuma, H. Okumura, S. Misawa, K. Endo, and S. Yoshida, Growth of High-Mobility 3C-SiC Epilayers by Chemical Vapor Deposition, *Jpn. J. Appl. Phys.* **27**, L434 (1988).
 - [110] F. Meng, J. Ma, J. He, and W. Li, Phonon-limited carrier mobility and temperature-dependent scattering mechanism of 3C-SiC from first principles, *Phys. Rev. B* **99**, 045201 (2019).
 - [111] R. L. Petritz and W. W. Scanlon, Mobility of Electrons and Holes in the Polar Crystal, PbS, *Phys. Rev.* **97**, 1620 (1955).
 - [112] C. G. Fonstad and R. H. Rediker, Electrical Properties of High-Quality Stannic Oxide Crystals, *J. Appl. Phys.* **42**, 2911 (1971).
 - [113] A. R. Hutson, Hall Effect Studies of Doped Zinc Oxide Single Crystals, *Phys. Rev.* **108**, 222 (1957).

- [114] L.-D. Zhao, S.-H. Lo, Y. Zhang, H. Sun, G. Tan, C. Uher, C. Wolverton, V. P. Dravid, and M. G. Kanatzidis, Ultralow thermal conductivity and high thermoelectric figure of merit in SnSe crystals, *Nature* **508**, 373 (2014).
- [115] J. Ma, Y. Chen, and W. Li, Intrinsic phonon-limited charge carrier mobilities in thermoelectric SnSe, *Phys. Rev. B* **97**, 205207 (2018).
- [116] C. Jacoboni, C. Canali, G. Ottaviani, and A. Alberigi Quaranta, A review of some charge transport properties of silicon, *Solid State Electron.* **20**, 77 (1977).
- [117] S. K. Sutadhar and D. Chattopadhyay, Thermoelectric power of n-GaAs, *J. Phys. C: Solid State Phys.* **12**, 1693 (1979).
- [118] A. Amith, I. Kudman, and E. F. Steigmeier, Electron and Phonon Scattering in GaAs at High Temperatures, *Phys. Rev.* **138**, A1270 (1965).
- [119] C. Sułkowski, A. ChuchmaŁa, A. J. Zaleski, M. Matusiak, J. Mucha, P. GŁuchowski, and W. Stręk, Transport properties, specific heat and thermal conductivity of GaN nanocrystalline ceramic, *J. Solid State Chem.* **183**, 2501 (2010).
- [120] I. Kudman and E. F. Steigmeier, Thermal Conductivity and Seebeck Coefficient of InP, *Phys. Rev.* **133**, A1665 (1964).
- [121] K. Morikawa, Seebeck Effect in Cadmium Sulfide, *J. Phys. Soc. Jpn.* **20**, 786 (1965).
- [122] H. Wang, E. Schechtel, Y. Pei, and G. J. Snyder, High Thermoelectric Efficiency of n-type PbS, *Adv. Energy Mater.* **3**, 488 (2013).
- [123] D. F. Morgan and D. A. Wright, Electrical properties of single crystals of antimony-doped stannic oxide, *Br. J. Appl. Phys.* **17**, 337 (1966).
- [124] T. Tsubota, M. Ohtaki, K. Eguchi, and H. Arai, Thermoelectric properties of Al-doped ZnO as a promising oxide material for high-temperature thermoelectric conversion, *J. Mater. Chem.* **7**, 85 (1997).
- [125] T. H. Geballe and G. W. Hull, Seebeck Effect in Silicon, *Phys. Rev.* **98**, 940 (1955).
- [126] C. Herring, Theory of the Thermoelectric Power of Semiconductors, *Phys. Rev.* **96**, 1163 (1954).